3 Irradiation–Assisted Stress Corrosion Cracking of Austenitic Stainless Steel in BWRs

The susceptibility of austenitic SSs and their welds to IASCC as a function of the fluence level, water chemistry, material chemistry, welding process, and fabrication history is being evaluated. Crack growth rate (CGR) tests and slow strain rate tests (SSRTs) are being conducted on model SSs, irradiated at ≈288°C in a helium environment in the Halden boiling heavy water reactor, to investigate the effects of material chemistry and irradiation level on the susceptibility of SSs to IASCC. Crack growth tests will be conducted on irradiated specimens of submerged arc (SA) and shielded metal arc (SMA) welds of Types 304 and 304L SS to establish the effects of fluence level, material chemistry, and welding process on IASCC. Models and codes developed under CIR and from industry sources will be benchmarked and used in conjunction with this work. However, for crack–growth rate models for irradiated materials it is anticipated that relatively few data will be available because of the expense and difficulty of testing. Additional testing on nonirradiated materials will be performed to provide "limiting cases" against which the models can be tested. These tests will seek to determine the effects of chromium level in the steel and cold work on CGRs in austenitic SSs in LWR environments.

During this reporting period the results obtained in the present study from SSRT tests on irradiated austenitic SS alloys have been compared with data available in the literature. The IASCC–susceptible or –resistant behavior of austenitic SSs is represented in terms of a two–dimensional map of bulk S and C contents of the steels. Also, CGR data in BWR environments at 289°C are presented for (a) Heat C3 of Type 304L SS irradiated to 0.3×10^{21} n/cm^2 (0.45 dpa) and (b) nonirradiated SS weld HAZ specimens from the Grand Gulf (GG) reactor core shroud H5 weld and a laboratory–prepared weld.

3.1 Slow-Strain-Rate-Tensile Test of Model Austenitic Stainless Steels Irradiated in the Halden Reactor (H. M. Chung and R. V. Strain)

3.1.1 Introduction

Failures of some BWR and PWR core internal components have been observed after accumulation of fast neutron fluences higher than $\approx 0.5 \times 10^{21}$ n/cm^2 (E >1 MeV) (≈0.7 dpa) in BWRs and at fluences approximately an order of magnitude higher in PWRs. The general pattern of the observed failures indicates that as nuclear plants age and fluence increases, various nonsensitized austenitic stainless steels (SSs) become susceptible to intergranular (IG) failure. Failure of welded components (such as core shrouds fabricated from Type 304 or 304L SS) has also been observed in many BWRs, usually at fluence levels significantly lower than the threshold fluence for the solution-annealed base-metal components.

Although most failed components can be replaced, some safety–significant structural components (e.g., the BWR top guide, core shroud, and core plate) would be very difficult or costly to replace. Therefore, the structural integrity of these components has been a subject of concern, and extensive research has been conducted to gain an understanding of this type of degradation, which is commonly known as irradiation-assisted stress corrosion cracking (IASCC).[14–41]

Irradiation produces profound effects on local coolant water chemistry and component microstructure. Neutron irradiation causes alteration of microchemistry, microstructure, and mechanical properties of the core internal components, which are usually fabricated from ASTM Types 304, 304L, 316, or 348 SS. It produces defects, defect clusters, and defect-impurity complexes in grain matrices and

alters the dislocation and dislocation loop structures, leading to radiation-induced hardening, and in many cases, flow localization via dislocation channeling. It also leads to changes in the stability of second–phase precipitates and the local alloy chemistry near grain boundaries, precipitates, and defect clusters. Grain–boundary microchemistry significantly different from bulk composition can be produced in association with not only radiation–induced segregation, but also thermally driven equilibrium and nonequilibrium segregation of alloying and impurity elements.

Irradiation–induced grain–boundary depletion of Cr has been considered for many years to be the primary metallurgical process that leads to IASCC in BWRs. One of the most important factors that seem to support the Cr–depletion mechanism is the observation that the dependence on water chemistry (i.e., oxidizing potential) of intergranular stress corrosion cracking (IGSCC) of nonirradiated thermally sensitized material and of IASCC of BWR–irradiated solution–annealed material is similar.[14,17,18] Many investigators have also suggested that radiation–induced segregation of ASTM–specification allowable impurities such as Si and P and other minor impurities not specified in the ASTM specification[21–36] has a role in the IASCC process. However, the exact mechanism of IASCC still remains unknown.

In general, IASCC is characterized by strong heat-to-heat variation in susceptibility, even among materials of virtually identical chemical compositions. This suggests that the traditional interpretation based on the role of grain-boundary Cr depletion alone may not completely explain the IASCC mechanism. An irradiation test program is being conducted to investigate systematically the effects of alloying and impurity elements (Cr, Ni, Si, P, S, Mn, C, N, and O) on the susceptibility of austenitic stainless steels to IASCC at several fluence levels.

In previous studies, SSRT tests and fractographic analysis were conducted on model austenitic SS alloys irradiated at 289°C to a "low-fluence" level of ≈0.3 x 10^{21} n/cm^2 (E > 1 MeV) (≈0.43 dpa), "medium-fluence" level of ≈0.9 x 10^{21} n/cm^2 (E > 1 MeV) (≈1.3 dpa),[41,42] and a "high-fluence" level of ≈2.0 x 10^{21} n/cm^2 (E > 1 MeV) (≈3.0 dpa).[43] Ten of the 11 heats were austenitic SS, and one was austenitic-ferritic SS containing ≈3 vol.% ferrite of globular shape. This report presents a comparison of the results with data available in the literature. The IASCC–resistant or –susceptible behavior of austenitic SSs is represented in terms of a two–dimensional map of bulk S and C contents of the steels.

3.1.2 Representation of IASCC-Resistant or –Susceptible Behavior of 304- and 316-Type Steels in Sulfur-Carbon Map

Typical in-service cracking of BWR core internal components occurs at >2 dpa and is characterized by a virtually full IG fracture surface, sometimes accompanied by a small amount of TG fracture surface. In this respect, the IASCC behavior of SSs at ≈3 dpa is more relevant than that at ≈1.3 dpa. The IASCC–resistant or –susceptible behavior at ≈ 3 dpa is largely determined by the bulk concentrations of S and C. Similar analysis was performed for data reported in the literature.[17–20,25–38] Virtually all literature data have been reported after 1987. The two-dimensional map of bulk S and C contents in Figs. 19 and 20 show the range in which 304– or 316–type steels are either resistant or susceptible to IASCC. The figure also includes similar data reported in the literature since 1987. The only data missing from the figure are those obtained for BWR internals for which S and C contents are not available, e.g., an IASCC-resistant 304 SS control blade sheath reported in Ref. 40 and an IASCC-susceptible 304L SS dry tube reported by Shen and Chang.[44]

In constructing the maps in Figs. 19 or 20, we assumed that a heat susceptible at <2.5 dpa is equally or more susceptible at ≥3 dpa under otherwise similar conditions. We also assumed that a heat susceptible at a DO concentration of <0.4 ppm is more susceptible at a DO concentration of ≥8 ppm

under otherwise identical conditions. Note that, in these figures, the plotted ranges of S and C contents extend beyond the AISI limits specified for Type 304 and 316 SS, i.e., maximum S = 0.030 wt.% and maximum C = 0.08 wt.%.

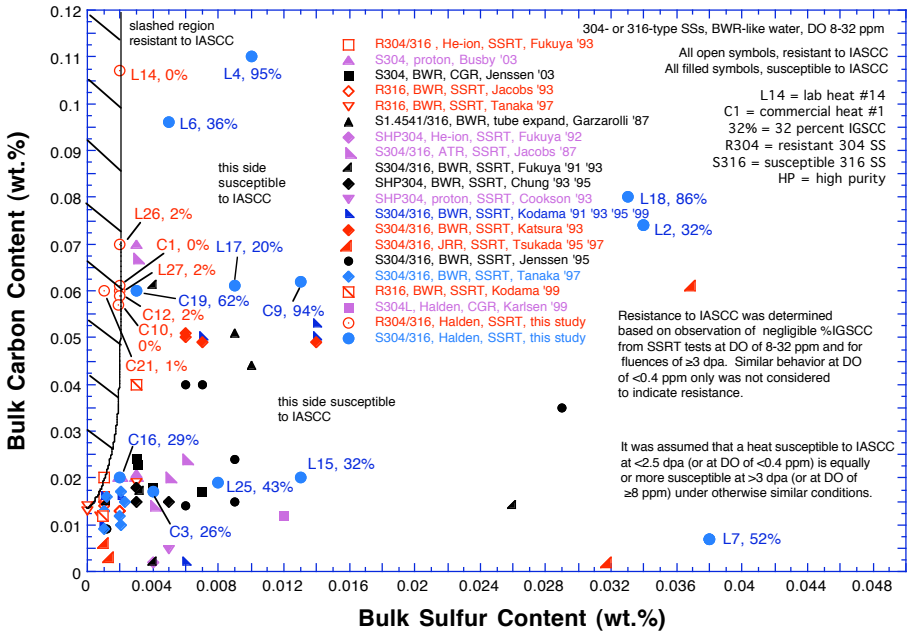

Figure 19. Range of bulk S and C contents in which 304- or 316-type steels are resistant or susceptible to IASCC in BWR-like oxidizing water.

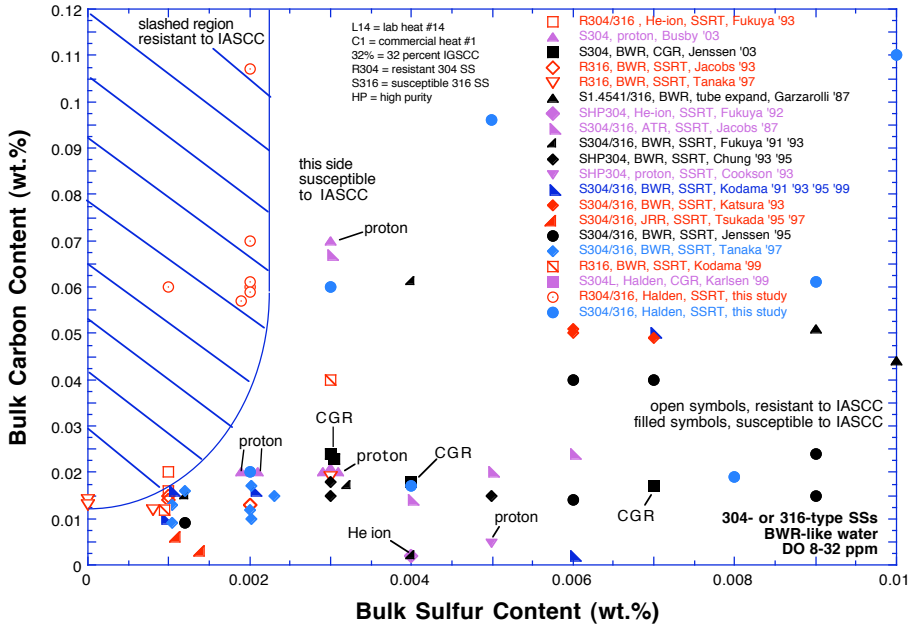

Figure 20. Expanded view of low-S portion of Fig. 19 showing data in detail.

In Figs. 19 and 20, data obtained on neutron-, ion-, or proton-irradiated steels from SSRT, CGR, or tube-expansion tests are shown for comparison with those obtained by SSRT in this investigation. As shown in Fig. 20, the results obtained on He–ion–irradiated steels by Fukuya et al.[25] and proton–irradiated steels by Cookson et al.[28] and Busby et al.[37] are also consistent with the IASCC–susceptible range shown in the S–C map. The earlier efforts by the latter group of investigators focused on "ultra-high-purity" (UHP) heats. However, their "UHP" heats contained either insufficiently low concentrations of S, insufficiently high concentrations of C, or both, to render the steel resistant to IASCC. Figure 20 also includes the results of CGR tests reported by Karlsen and Hauso[38] and Jenssen et al.,[35] in which IG crack propagation was confirmed by SEM fractography.

In Fig. 21, which is similar to Fig. 19, data points for four susceptible heats tested after irradiation to 1.3 dpa (i.e., Heats L22, L11, L13, and L8) are also included. It was assumed that the four heats are also susceptible to IASCC at 3 dpa, although they were not tested at this damage level.

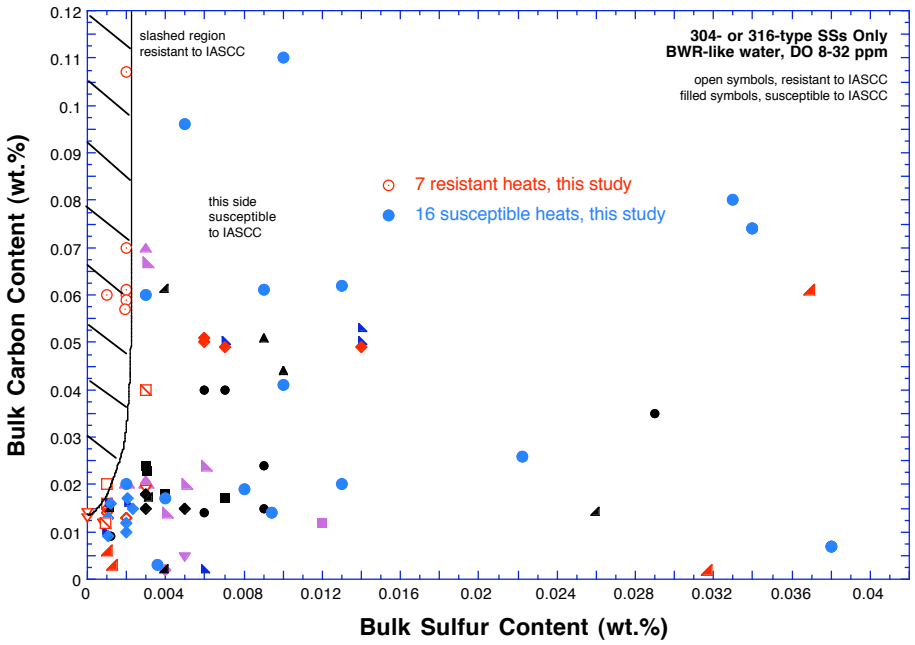

Figure 21. Range of bulk S and C contents in which 304– or 316–type steels are resistant or susceptible to IASCC, including four susceptible heats tested at 1.3 dpa in this study.

3.1.3 Grain-Boundary Segregation of Sulfur and Carbon

In the consideration of the importance of the roles of S and C in IASCC, the behavior of grain-boundary segregation of the two elements was characterized by Auger electron spectroscopy (AES). Similar analysis by advanced analytical electron microscopy (AAEM) is difficult or impractical for an ordinary grain boundary in an irradiated steel, although S-rich thin films on a crack-tip grain boundary can be detected.[45,46] Auger electron spectroscopy is probably the only practical technique that can characterize adequately the profile and degree of grain-boundary segregation of S and C in an irradiated steel.

The materials selected for the AES analysis were taken from BWR neutron absorber tubes. The absorber tubes were fabricated from two commercial heats of Type 304 SS (Heats A and B) and were

irradiated to 2.0 x 10^{21} n/cm^2 (E > 1 MeV) (≈3 dpa) during service in a BWR. The behavior of grain-boundary segregation in such material was considered most relevant to BWR IASCC. The neutron absorber tubes were susceptible to field cracking. Unfortunately, neither documented chemical composition of the absorber tubes nor the archive, unirradiated ingots could be found.

Needle-like specimens were prepared from the selected BWR neutron absorber tubes. After cathodically charging with hydrogen at ≈50°C in a solution that contained 100–mg/L $NaAsO_2$ dissolved in 0.1–N H_2SO_4, the needle-like specimen was fractured in a 23°C vacuum in a scanning Auger electron microscope (SAM). In-situ analysis was performed in a JEOL JAMP–10 SAM equipped with automated Ar-sputtering and depth-profiling devices. Four to six ductile fracture surfaces and 12–15 IG fracture surface locations were selected for spot analysis in each specimen. Sulfur and C signals from the selected surfaces were then recorded and compared.

After each spot analysis, a depth-profile analysis was performed on a selected IG fracture surface. The procedure for automated depth-profiling analysis has been described elsewhere.[23,27] Progressive sputtering of the intergranular surfaces with Ar ions and acquisition of the Auger electron signals in the ultra-high vacuum environment of the SAM were controlled by computer.

An example of an IG fracture surface, produced at 23°C in the H-charged specimens from an absorber tube (304 SS Heat B), is shown in Fig. 22. The IG fracture surfaces reveal numerous deformation steps and a precipitate (diameter ≈15 μm) denoted with the number "6". Spots denoted with numbers "5" and "20" were selected for acquisition of Auger electron signals. The results of spot analyses obtained for Tubes A-1 and B are shown in Figs. 23 and 24, respectively. In Fig. 23a, the peak heights of Auger electrons of S obtained from four ductile fracture surfaces are presented with their counterparts from 12 IG fracture surfaces in Tube A-1. The S intensities from the IG fracture surfaces are significantly higher than their counterparts from ductile-fracture surfaces (i.e., spots not on a grain boundary). This behavior shows that S segregated significantly to grain boundaries (i.e., IG fracture surface) in Tube A-1. Similar results for C are also plotted in Fig. 23b, which shows that C segregated significantly to grain boundaries in the same tube. Essentially the same behavior was observed for S and C segregation in Tube B; see Fig. 24.

A careful examination of Figs. 23 and 24 reveals that some spots that contain high concentrations of S also contain high concentration of C, e.g., intergranular Spot 16, Tube A-1, and intergranular Spot

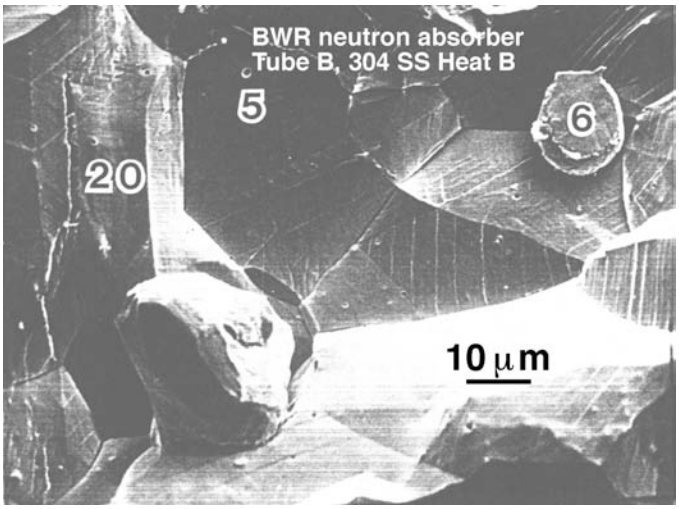

Figure 22. High-magnification fractograph of H-charged BWR neutron absorber tube, 304 SS, Heat B, ≈3 dpa; fracture was produced at 23°C in ultra-high vacuum environment in a scanning Auger electron microscope.

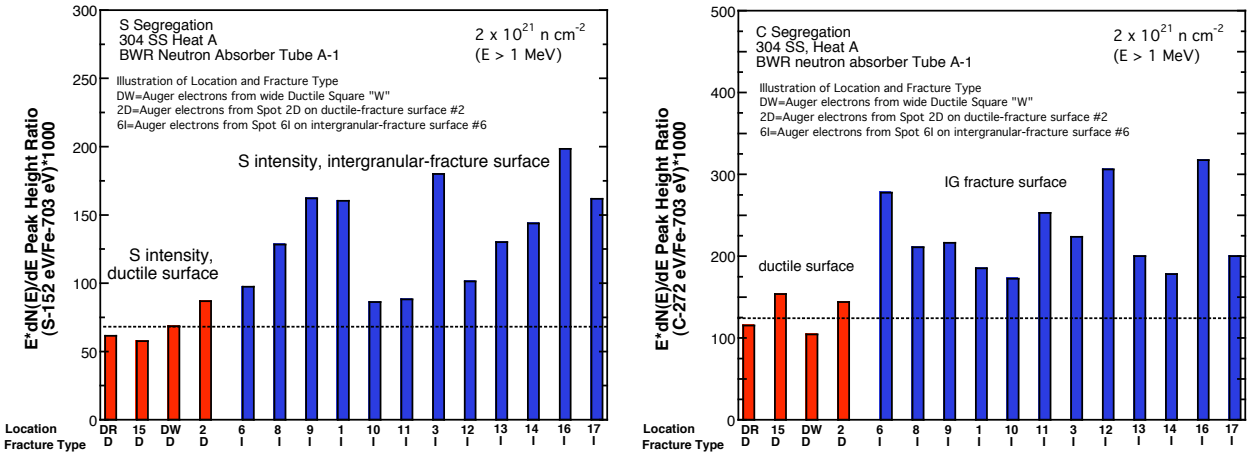

(a) (b)

Figure 23. Summary of AES analysis of grain-boundary segregation of S (a) and C (b) in BWR neutron absorber tube fabricated from Type 304 SS Heat A and irradiated to 3 dpa: S and C peak heights from ductile (denoted "D") and IG (denoted "I") fracture surfaces are compared.

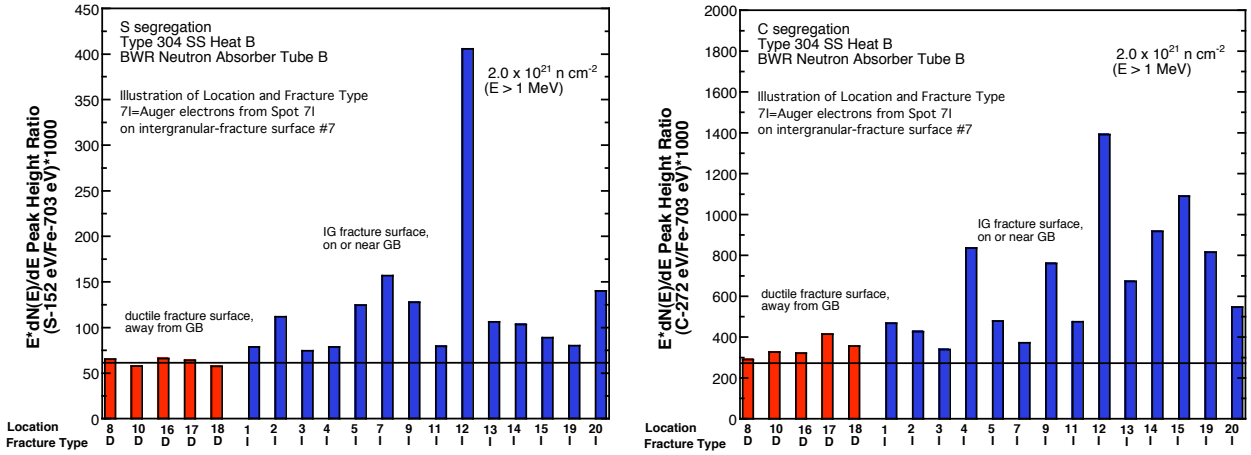

(a) (b)

Figure 24. Summary of AES analysis of grain-boundary segregation of S (a) and C (b) in BWR neutron absorber tube fabricated from Type 304 SS Heat B and irradiated to 3 dpa: S and C peak heights from ductile (denoted "D") and IG (denoted "I") fracture surfaces are compared.

12, Tube B. However, whether C segregates preferentially to a grain-boundary region that contains a high concentration of S, or vice versa, is not conclusive. This behavior could not be conclusively determined by AES in this investigation; it needs further study by a more direct technique such as the field-emission atom-probe technique.

Figure 25 shows the results of depth-profile analysis for the two tubes fabricated from 304 SS Heats A-1 and B. The figure confirms significant grain-boundary segregation of S in Tubes A-1 and B and C segregation in Tube B.

The results in Figs. 22–25, however, do not clarify whether the grain-boundary segregation of S or C occurred via a thermal process (during fabrication), an irradiation-induced process, or both. The former

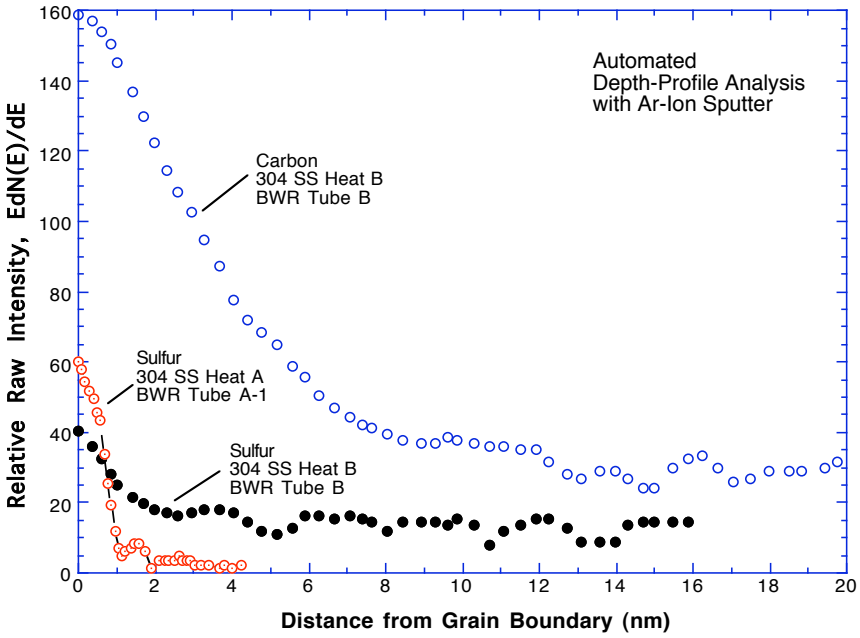

Figure 25. Result of AES depth-profiling analysis of grain-boundary segregation of S and C in BWR neutron absorber tubes fabricated from Type 304 SS Heats A and B and irradiated to ≈3 dpa.

type of segregation is expected to be significantly influenced by several steps during fabrication, e.g., ingot cooling, inter-rolling annealing and cooling, final annealing, and quenching. Thermal segregation is also influenced by plate thickness.

Results of AES analysis of grain-boundary segregation of S have been reported by Jacobs et al.[47] for fuel-cladding-like tubes that were irradiated in a BWR. A tube fabricated from a commercial heat of Type 348 SS was irradiated to 1.5 x 10^{21} n·cm^{-2} (E > 1 MeV), and a tube fabricated from a high-purity heat of Type 348 SS was irradiated to 3.4 x 10^{21} n·cm^{-2} (E > 1 MeV). Results of spot analyses, similar to those of Figs. 23 and 24, showed significant grain–boundary segregation of S in both tubes. Depth-profiling analysis similar to that of Fig. 25 was, however, not reported from their investigation.

Andresen and Briant reported on the thermal segregation of S in grain boundaries for unirradiated ultra–high purity (UHP) austenitic SS doped with S.[48] They concluded that S plays an important role in producing the IG crack path in thermally sensitized non-irradiated steels. Because S atoms are thermally segregated on grain boundaries, more S ions are released into water from the grain boundary than from the grain matrix, and it was thought that an IG crack path is promoted in steels that contain high concentrations of S. Thus, the authors essentially viewed the role of S as accelerating corrosive attack (i.e., dissolution of grain boundary metal) of a Cr-depleted grain boundary, exacerbated by S ions released into the crack tip water. According to this model, as long as grain boundaries are significantly depleted of Cr, the production of an IGSCC path is predicted, even in a steel free of S.

However, a similar model of the role of S does not appear to explain our results on IASCC susceptibility of irradiated steels. One difficulty is how to explain the observation that IASCC susceptibility becomes negligible when S concentration is very low even though Cr depletion is

significant at ≈3 dpa. Another difficulty is how to explain the trend that the S effect is strongly influenced by fluence at >0.003 wt.% S, e.g., in 304- and 316-type steels.

3.1.4 Analysis of Solubility of Carbon in Sulfides

The results in Figs. 19–21 indicate that, when S concentration in 304– or 316–type steel is ≤0.002 wt.%, a high concentration of C (>0.03 wt.%) promotes a decrease of the susceptibility to IASCC. When S concentration exceeds ≈0.003 wt.%, such a "beneficial" effect of high C concentration appears to be insignificant or absent. This observation suggests a relationship between S and C, and that the effect of this relationship is significant only at sufficiently low concentrations of S (<0.002 wt.%).

With respect to the above observation, our attention was focused on the composition and properties of Ni– and S–rich thin films that were observed on grain boundaries under three situations: at crack–tip grain boundaries in an nonirradiated thermally sensitized crack–growth specimen tested in sulfated BWR–like water (304 SS), reported by Dumbill;[49] at crack-tip grain boundaries in a field–failed BWR top guide and a PWR baffle bolt (Type 304 SS), reported by Thomas and Bruemmer;[45,46] and at ordinary grain boundaries of S-doped Ni specimens that failed during SSRT tests in air at 23°C, reported by Heuer et al.[50] The latter investigators showed that S–doped Ni specimens lose their tensile strength when the grain-boundary concentration of S exceeds ≈15 at.%, which causes an IG failure. Then, it was thought in our study that, if C is dissolved in a Ni_xS_y–type film in a significant amount, the mechanical properties of such a film are likely to be altered significantly. Accordingly, available information and data were evaluated to determine if C is soluble in sulfides.

The AES signal from the precipitate denoted with number "6" in Fig. 22 is shown in Fig. 26. The AES signal indicates that the precipitate is a CuS-type that contains a significant amount of C. Similar data are shown in Figs. 27 and 28 for two more CuS-type precipitates that were present in the same specimen.

The only direct evidence of significant solubility of C in Ni sulfide could be observed from the data reported by Dumbill.[49] The data obtained by field-emission-gun advanced analytical electron microscopy (FEG-AAEM) show X-ray intensities of Ni, S, and C contained in a Ni- and S-rich thin film that was

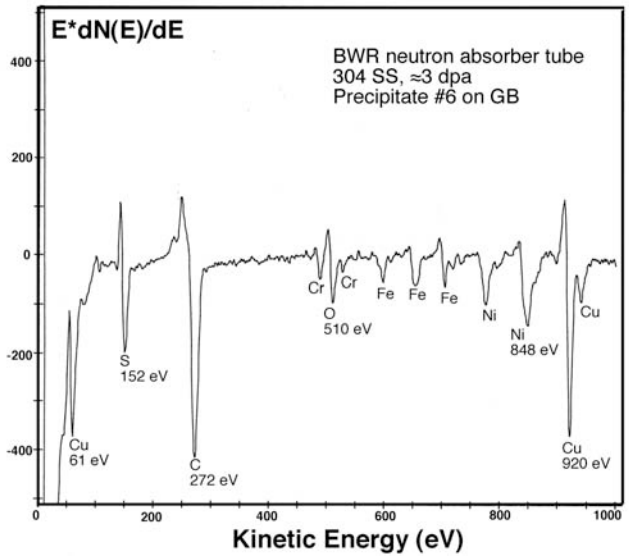

Figure 26.
AES signal showing high concentrations of Cu, S, and C in CuS-type precipitate denoted with number "6" in Fig. 22.

observed at an intergranular crack in a thermally sensitized, unirradiated Type 304 SS. The FEG-AAEM X-ray spectra strongly indicate that C can be dissolved in significant amounts in Ni- and S-rich thin films at ≈290°C. Unfortunately, similar data were not reported for the field-cracked (irradiated) steels examined by Thomas and Bruemmer.[45,46] However, irradiation is not expected to significantly decrease the solubility of C in the Ni- and S-rich thin films or islands that they observed.

Based on the information described above, it is predicted that C atoms compete with S atoms to become incorporated in the unit cell of NiS-type sulfides under BWR conditions. The degree of such C incorporation, which replaces part of the S atoms in the sulfide, is predicted to be more pronounced for a higher concentration of C at the grain boundary, i.e., for a high C content in the steel and for a higher degree of grain-boundary segregation of C.

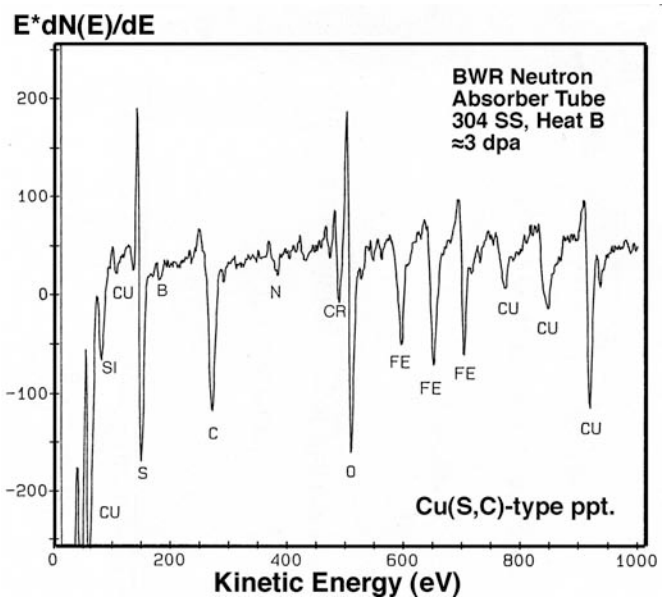

Figure 27.
AES signal showing a high concentration of C in CuS-type precipitate in BWR neutron absorber tube, 304 SS, Heat B, ≈3 dpa.

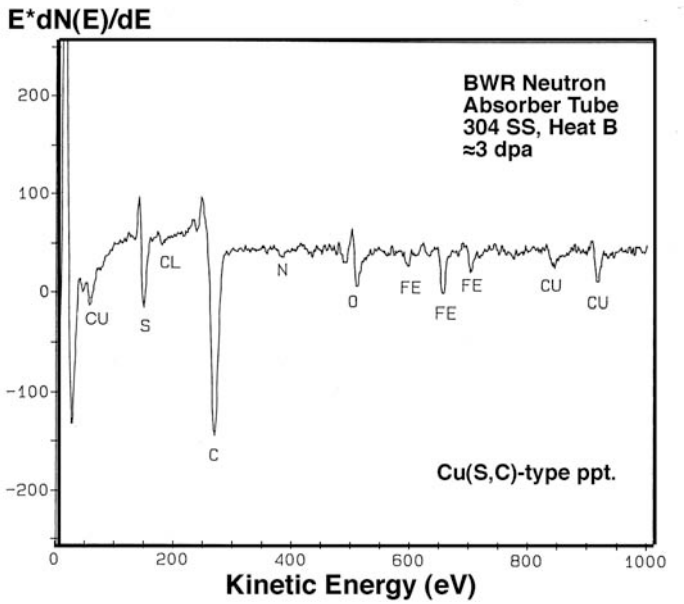

Figure 28.
AES signal showing a high concentration of C in another CuS-type precipitate in BWR neutron absorber tube, 304 SS, Heat B, ≈3 dpa.

3.2 Crack Growth Rate Test of Austenitic Stainless Steels Irradiated in the Halden Reactor (E. E. Gruber and O. K. Chopra)

3.2.1 Introduction

Austenitic stainless steels (SSs) are used extensively as structural alloys in reactor pressure vessel internal components because of their high strength, ductility, and fracture toughness. However, exposure to neutron irradiation for extended periods changes the microstructure and degrades the fracture properties of these steels. Irradiation leads to a significant increase in yield strength and a reduction in ductility and fracture resistance of austenitic SSs.[51–54] Radiation can exacerbate the corrosion fatigue and stress corrosion cracking (SCC) behavior of SSs[51,55,56] by affecting the material microchemistry, e.g., radiation–induced segregation; material microstructure, e.g., radiation hardening; and water chemistry, e.g., radiolysis.

The factors that influence SCC susceptibility of materials include neutron fluence, cold work, corrosion potential, water purity, temperature, and loading. The effects of neutron fluence on irradiation assisted stress corrosion cracking (IASCC) of austenitic SSs have been investigated for BWR control blade sheaths[57–59] and laboratory tests on BWR–irradiated material;[55,60–62] the extent of intergranular SCC increases with fluence. Although a threshold fluence level of 5×10^{20} n/cm^2 (E >1 MeV)* (≈0.75 dpa) has been proposed for austenitic SSs in BWR environments based on early experimental results, intergranular cracking has been seen at fluences as low as ≈2×10^{20} n/cm^2 (≈0.3 dpa).[55,63] The results also show the beneficial effect of reducing the corrosion potential of the environment,[64,65] which suggests that the threshold fluence for IASCC is higher under low potential conditions such as BWR hydrogen water chemistry (HWC) or PWR primary water chemistry. However, low corrosion potential does not provide immunity to IASCC if the fluence is high enough.[35]

This program is being conducted at ANL on irradiated SSs to support the regulatory request to understand better the safety issues attendant to the cracking of BWR internals such as core shrouds. The susceptibility of austenitic SSs to IASCC is being evaluated as a function of the fluence level, material composition, and water chemistry. Crack growth rate (CGR) tests are being conducted on Type 304 and 316 SS base metal and weld heat affected zones (HAZ) irradiated to fluence levels up to 2.0×10^{21} n/cm^2 (3.0 dpa) at ≈288°C. The CGR tests are conducted in normal water chemistry (NWC) and hydrogen water chemistry (HWC) BWR environments at ≈289°C.

Crack growth tests have been completed on Type 304L and 316L SS (Heats C3 and C16, respectively) irradiated to a fluence level of 0.9 and 2.0×10^{21} n/cm^2 (1.35 and 3.0 dpa). The results indicate significant enhancement of CGRs for irradiated steels in the NWC BWR environment.[66] Crack growth rates a factor of ≈5 higher than the disposition curve proposed in NUREG–0313[67] for sensitized austenitic SSs in water with 8 ppm dissolved oxygen (DO) have been observed. The CGRs of Type 304L SS irradiated to 1.35 and 3.0 dpa and of Type 316L SS irradiated to 3 dpa were comparable.

The results also indicated that in low–DO BWR environments, the CGRs of the irradiated steels decreased by an order of magnitude in some tests, e.g., Type 304L SS irradiated to 0.9×10^{21} n/cm^2 and Type 316L SS irradiated to 2×10^{21} n/cm^2. As noted previously, the benefit of low DO appears to decrease with increasing fluence. A threshold of about 5×10^{21} n/cm^2 has been suggested.[55,63] However, the beneficial effect of decreased DO was not observed in a test on Type 304L SS irradiated to

* All references to fluence levels are calculated for E ≥1 MeV.

2×10^{21} n/cm^2, although this different behavior may be associated with the loss of constraint in the specimen due to the high applied–load.[66]

This section presents experimental CGR data concerning BWR environments at 289°C for Heat C3 of Type 304L SS irradiated to 0.45 dpa. For comparison, baseline data have also been obtained on nonirradiated SS weld HAZ specimens obtained from Type 304L SS weld from the Grand Gulf (GG) reactor core shroud and a Type 304 SS laboratory–prepared weld.

3.2.2 Experimental

3.2.2.1 Specimen Geometry and Materials

The CGR tests were performed at ≈289°C on 1/4–T compact tension (CT) specimens in simulated BWR environments in accordance with ASTM E–647, "Standard Test Method for Measurement of Fatigue Crack Growth Rates", and ASTM E–1681, "Standard Test Method for Determining a Threshold Stress Intensity Factor for Environment–Assisted Cracking of Metallic Materials under Constant Load." The configuration of the specimens is shown in Fig. 29. Crack extensions were determined by DC potential measurements. The composition of Type 304L Heat C3 is presented in Table 3, and the tensile yield and ultimate stresses for the steel irradiated to three fluence levels and in the nonirradiated condition[41,42] are given in Table 4.

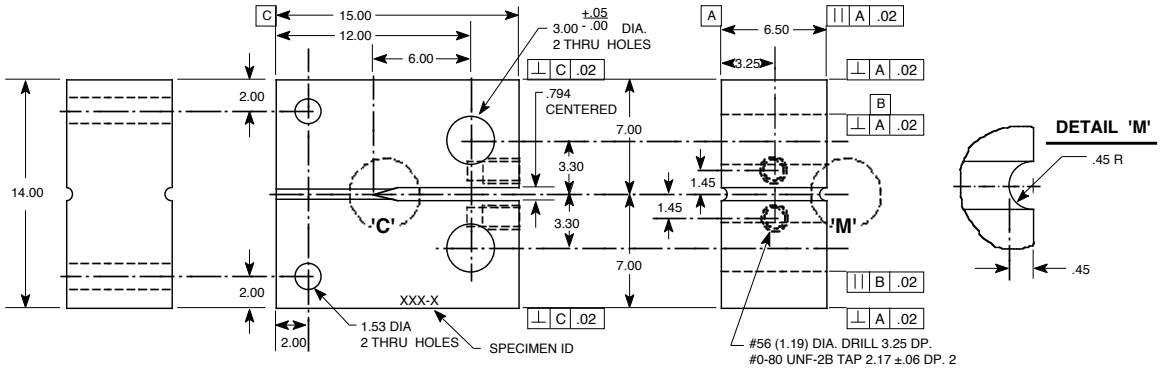

Figure 29. Configuration of compact–tension specimen for this study (dimensions in mm).

Table 3. Composition (wt.%) of Heat C3 of Type 304L stainless steel irradiated in the Halden reactor.

ID[a]	Heat ID	Analysis	Ni	Si	P	S	Mn	C	N	Cr	Mo	O[b]
C3	PNL-C-6	Vendor	8.91	0.46	0.019	0.004	1.81	0.016	0.083	18.55	–	–
		ANL	9.10	0.45	0.020	0.003	1.86	0.024	0.074	18.93	–	144

[a]First letters "C" denotes commercial heat.
[b]In wppm.

Table 4. Tensile properties (MPa) of irradiated Heat C3 of Type 304L stainless steel at 288°C.

			Fluence (E > 1 MeV)					
	Nonirradiated		0.3 x 10^{21} n/cm^2		0.9 x 10^{21} n/cm^2		2.0 x 10^{21} n/cm^2	
Steel Type (Heat)	Yield	Ultimate	Yield	Ultimate	Yield	Ultimate	Yield	Ultimate
304 SS (C3)	(154)[a]	(433)[a]	338	491	632	668	796	826

[a]Estimated value.

The HAZ specimens were obtained from the H5 core–shroud weld of the cancelled GG reactor and a shielded metal arc (SMA) weld prepared from a 30–mm plate of Type 304 SS (Heat 10285). The GG weld was fabricated from an SA 240 Type 304L hot–rolled plate using a double–V joint design. This plate had been welded by submerged arc (SA) method and ER308L filler metal. The SMA weld was prepared in the laboratory by welding two 70 x 178 mm (2.75 x 7.0 in.) pieces of 30 -mm thick (1.18 -in. thick) plate. The weld had a single V-joint design and was produced by 31 weld passes using E308 filler metal. Passes 1–5 were produced with 3.2 -mm (0.125 -in.) filler metal rod and 178 -mm/min (7 -ipm) travel speed, and passes 6–31 were produced with 4.0 -mm (0.156 -in.) filler metal rod and 216 -mm/min (8.5 -ipm) travel speed. Between passes the weld surfaces were cleaned by wire brush and grinding and rinsed with de–mineralized water or alcohol. The composition of Type 304 SSs used in the present study is presented in Table 5. The specimens were machined from 9.5–mm thick slices of the weld; some slices were thermally treated for 24 h at 500°C before machining. For all specimens, the machined notch was located in the HAZ of the weld. Each slice was etched, and the specimen orientation and notch location relative to the weld was clearly identified, Fig. 30.

Table 5. Composition (wt.%) of Type 304 stainless steels investigated.

Steel Type	Heat ID	Analysis	Ni	Si	P	S	Mn	C	N	Cr	Mo	O
304	10285	Vendor	8.40	0.51	0.032	0.006	1.64	0.058	–	18.25	0.41	–
		ANL	8.45	0.60	0.015	0.007	1.90	0.070	0.084	18.56	0.51	0.013
304L	GG Top Shell	ANL	9.05	0.53	0.027	0.016	1.84	0.013	0.064	18.23	0.44	0.010
	GG Bottom Shell	ANL	8.95	0.55	0.023	0.008	1.80	0.015	0.067	18.62	0.31	0.014

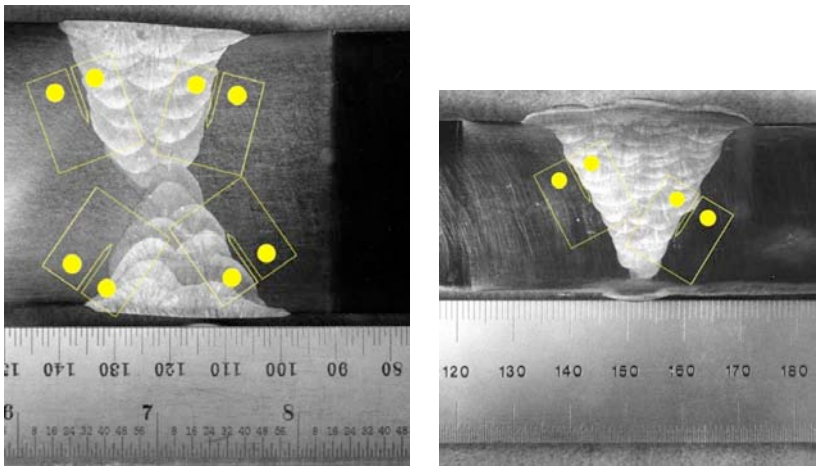

(a) (b)

Figure 30. Orientation of the 1/4–T CT specimens from the (a) Grand Gulf H5 SA weld HAZ and (b) laboratory–prepared SMA weld HAZ.

The microstructures of the base metal and as–welded HAZ of Type 304L SS from the GG top and bottom shells and Heat 10285 of Type 304 SS are shown in Figs. 31–36. The base metal of all the SSs contains stringers of ferrite, e.g., Figs. 31, 33, and 35; Heat 10285 appears to have the most amount of ferrite and the GG bottom shell the least amount. The grain sizes for the GG top and bottom shell materials are comparable and are larger than those for Heat 10285, e.g., the grain size in the HAZ region of the GG shell is ≈110 μm and that of Heat 10285 is ≈80 μm. In all welds, the fusion line extends into the base metal along the ferrite stringers, e.g., Figs. 32, 34, and 36. In other words, the ferrite stringers intersecting the fusion line appear to have melted and re–solidified during the welding process.

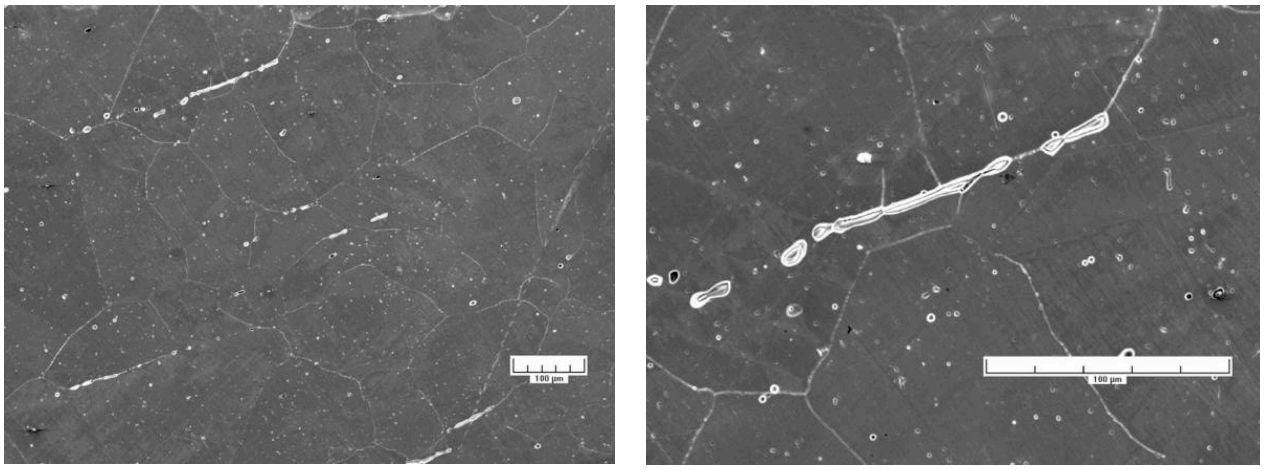

(a) (b)

Figure 31. (a) Low- and (b) high–magnification photomicrographs of the structure of the Type 304L base metal from the top shell of the H5 weld of the Grand Gulf core shroud.

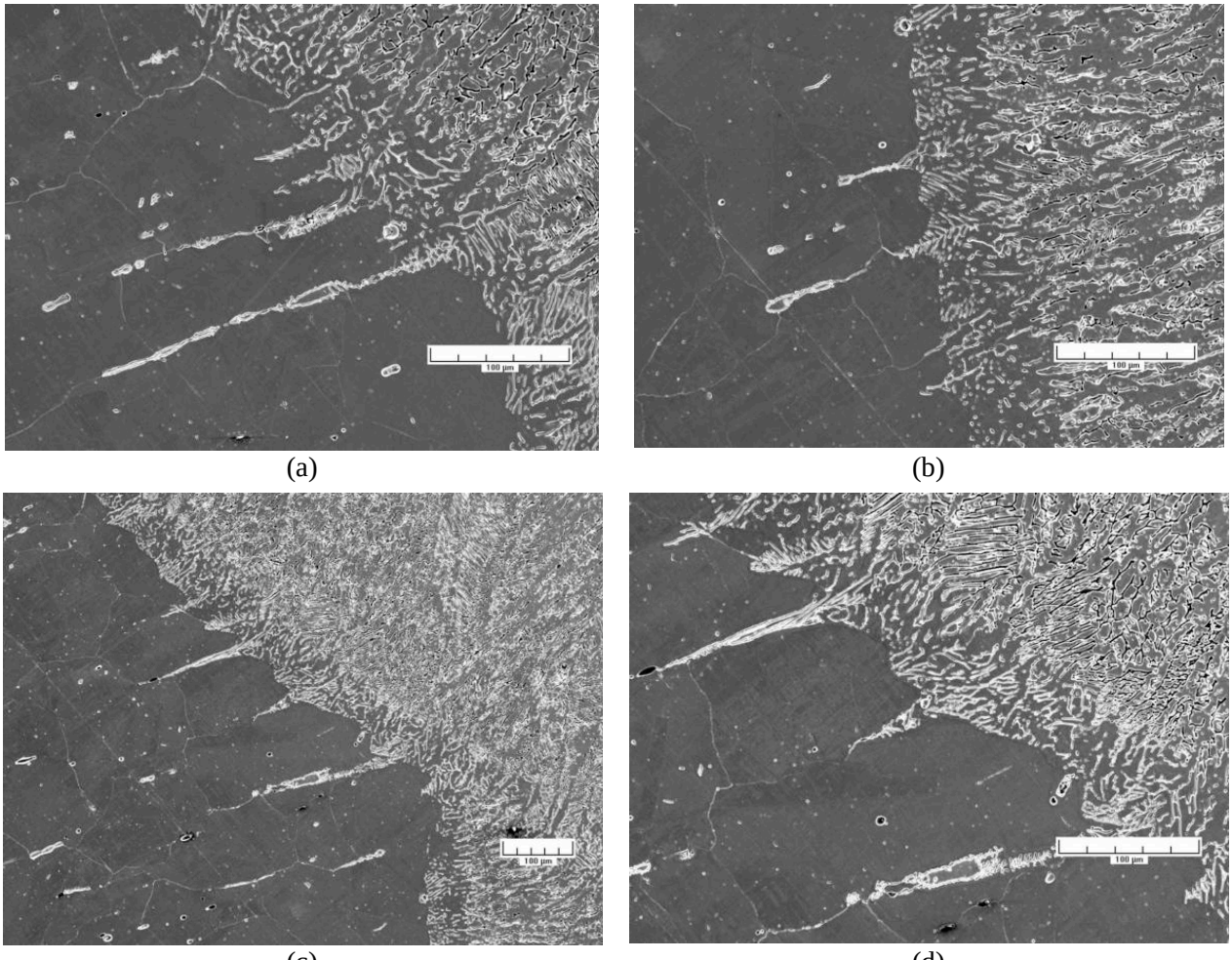

(a) (b)

(c) (d)

Figure 32. Micrographs of the interface between the weld metal and top shell of the H5 weld of the Grand Gulf core shroud.

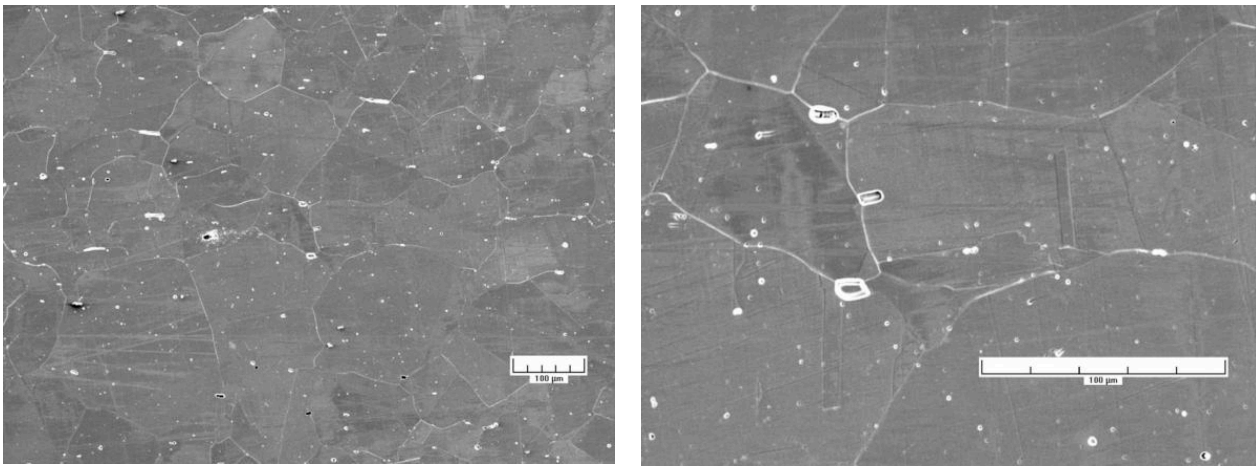

(a) (b)

Figure 33. (a) Low- and (b) high–magnification photomicrographs of the structure of the Type 304L base metal from the bottom shell of the H5 weld of the Grand Gulf core shroud.

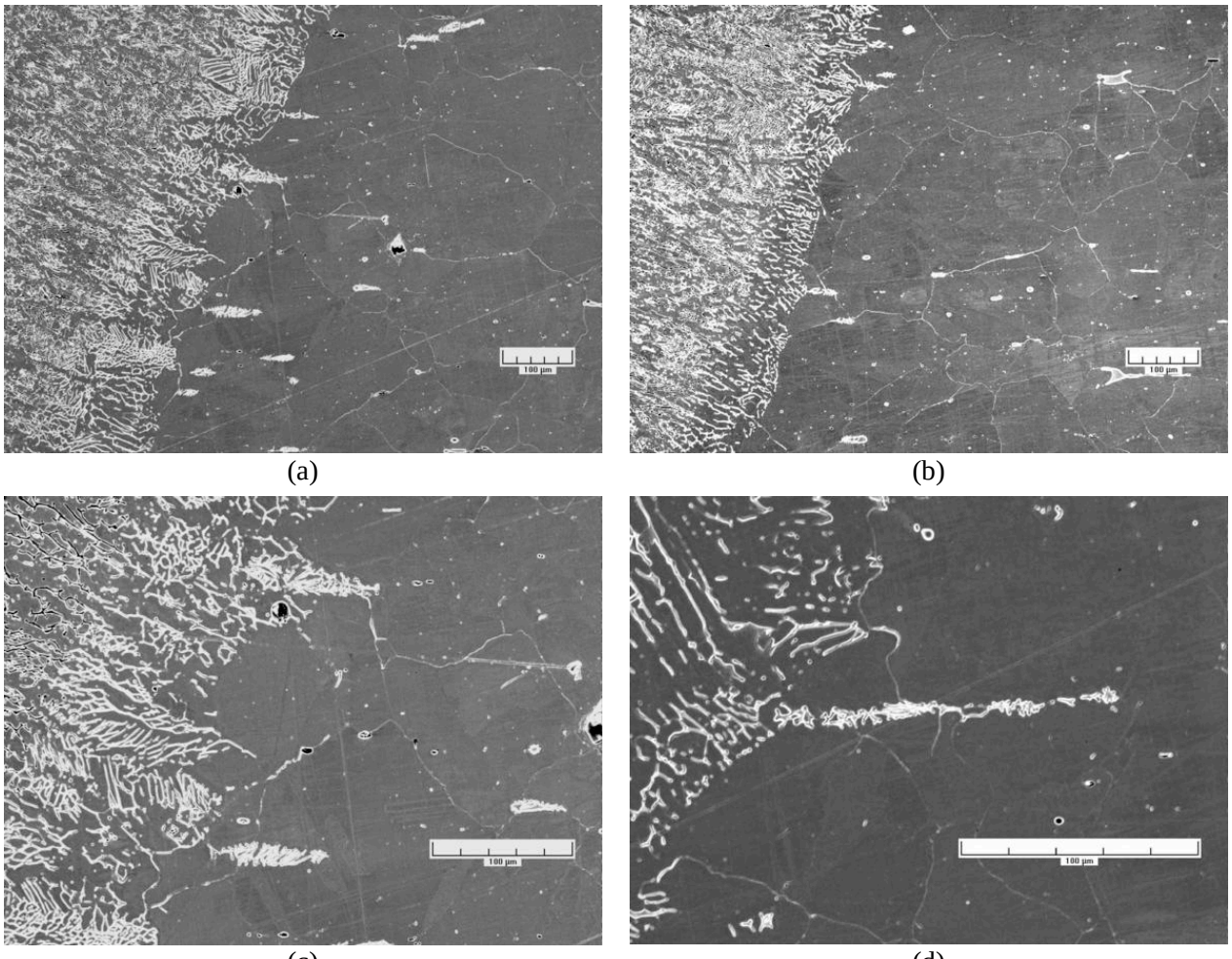

(a) (b)

(c) (d)

Figure 34. Micrographs of the interface between the weld metal and bottom shell of the H5 weld of the Grand Gulf core shroud.

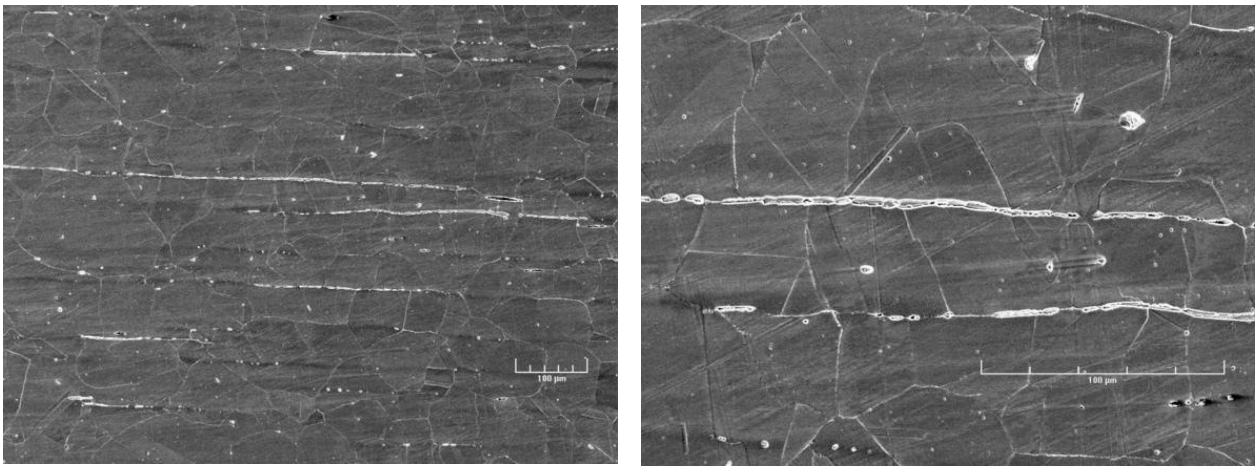

(a) (b)

Figure 35. (a) Low- and (b) high–magnification photomicrographs of the structure of Heat 10285 of the Type 304 base metal from the top shell of the H5 weld of the Grand Gulf core shroud.

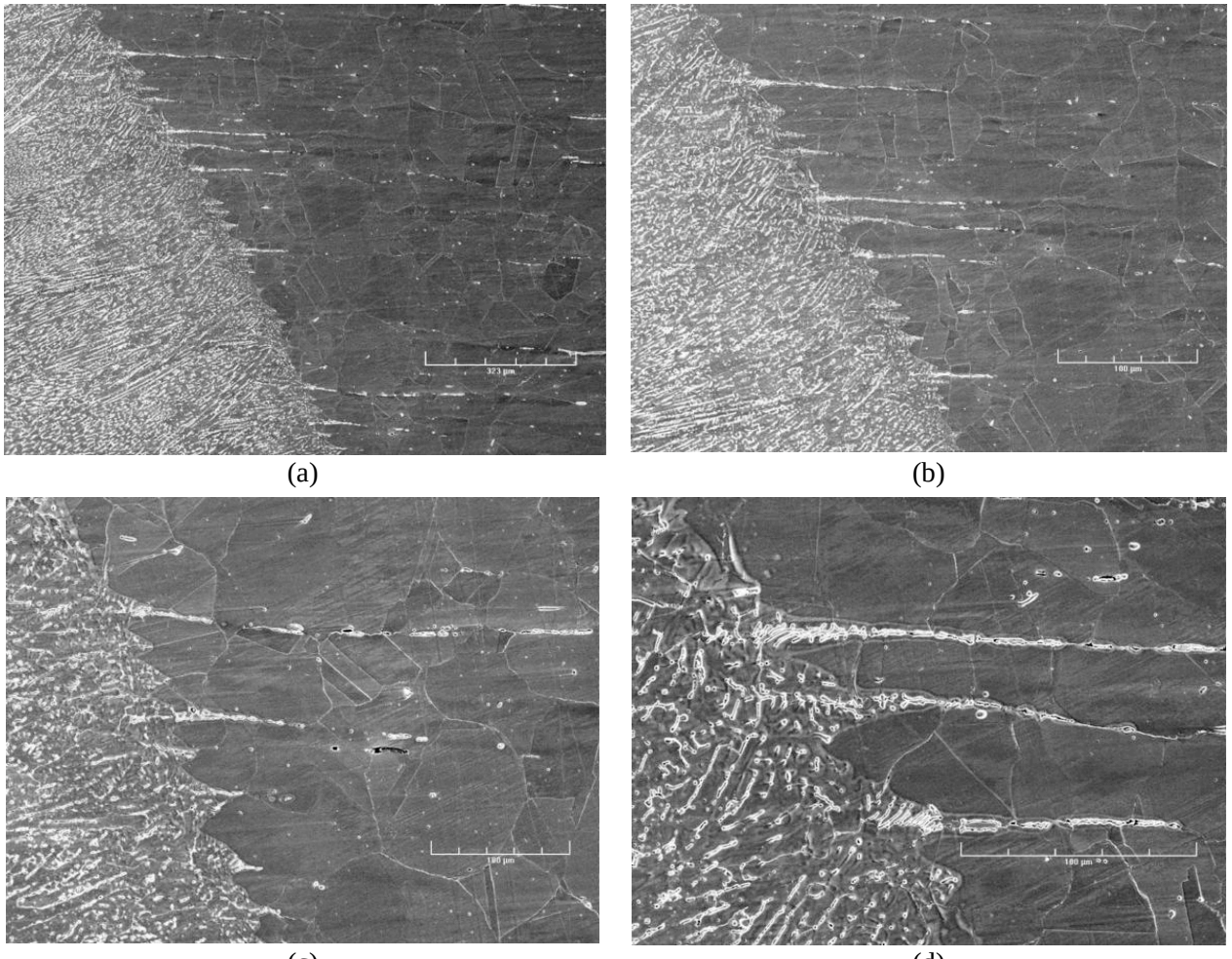

(a) (b)

(c) (d)

Figure 36. Micrographs of the interface between the weld metal and base metal.

The tensile properties of the GG core–shroud shell and Heat 10285, in the mill–annealed condition and after sensitization at 600°C for 10.5 h, are listed in Table 6. The tests were conducted on cylindrical specimens, 5.1 -mm diameter and 20.3 -mm gauge length, in air at 289°C and 0.008 %/s strain rate. The sensitization heat treatment has little effect on the tensile strength of the GG steel, whereas the strength of Heat 10285 is decreased. The tensile properties of the sensitized material are used to determine the K/size criterion for nonirradiated HAZ specimens, both in the as–welded and as–welded plus thermally treated conditions.

Table 6. Tensile properties of the austenitic stainless steels irradiated in the Halden reactor.

		Nonirradiated	
Steel Type	Material Condition	Yield (MPa)	Ultimate (MPa)
304 SS Heat 10285	Mill annealed	196	508
	MA + 10.5 h at 600°C	156	501
304L SS GG Core Shroud	Mill annealed	158	411
	MA + 10.5 h at 600°C	159	425

3.2.2.2 Test Procedure

The facility for conducting the tests is designed for in–cell testing, with the hydraulic actuator, test load train, autoclave, and furnace mounted on top of a portable wheeled cart that can be easily rolled into the cell. A detailed description of the facility is presented elsewhere.[68] The CGR tests were performed in accordance with ASTM E–647, "Standard Test Method for Measurement of Fatigue Crack Growth Rates", and ASTM E–1681, "Standard Test Method for Determining a Threshold Stress Intensity Factor for Environment–Assisted Cracking of Metallic Materials under Constant Load."

The CGR tests were started in high–purity water that contained 250–500 ppb DO (i.e., NWC BWR environment). The electrochemical potentials (ECPs) of a Pt electrode and a SS sample located at the exit of the autoclave were monitored continuously during the test; the water DO level and conductivity were determined periodically. After data were obtained for high–DO water, the DO level in the feedwater was decreased to <30 ppb by sparging it with pure N_2 or N_2 + 5% H_2. Because of the very low water flow rates, several days were required for the environmental conditions to stabilize for the in–cell tests. In general, the changes in ECP of the SS sample were slower than in the ECP of the Pt electrode. Because of the higher flow rates the changes in water chemistry for the out–of–cell tests were significantly faster.

All specimens were fatigue precracked in the test environment at load ratio R = 0.2–0.3, frequency of 1–5 Hz, and maximum stress intensity factor $K_{max} \approx 15$ MPa $m^{1/2}$. After 0.3–0.5 mm crack extension, a prescribed loading sequence was followed to facilitate the transition of a TG fatigue crack to a IG stress corrosion crack. To achieve this transition, R was increased incrementally to 0.7, and the loading waveform changed to a slow/fast sawtooth with rise times of 30–1000 s. The loading history was then changed to a trapezoidal waveform, R = 0.7, hold period at peak of 1 or 2 h, and unload/reload period of 24 s to measure SCC growth rates. For some specimens, CGRs were also obtained under constant load. During individual test periods, K_{max} was maintained approximately constant by periodic load shedding (less than 2% decrease in load at any given time).

Under cyclic loading, the CGR (m/s) can be expressed as the superposition of the rate in air (i.e., mechanical fatigue) and the rates due to corrosion fatigue and SCC, given as

$$\dot{a}_{env} = \dot{a}_{air} + \dot{a}_{cf} + \dot{a}_{SCC}. \quad (2)$$

The CGRs in air, $\dot{a}_{air}$ (m/s), were determined from the correlations developed by James and Jones;[69] it is expressed as

$$\dot{a}_{air} = C_{SS}\, S(R)\, \Delta K^{3.3}/T_R\,, \tag{3}$$

where R is the load ratio (K_{min}/K_{max}), ΔK is $K_{max} - K_{min}$ in MPa $m^{1/2}$, T_R is the rise time (s) of the loading waveform, and the function S(R) is expressed in terms of the load ratio R as follows:

$$\begin{aligned} S(R) &= 1.0 && R < 0 \\ S(R) &= 1.0 + 1.8R && 0 < R < 0.79 \\ S(R) &= -43.35 + 57.97R && 0.79 < R < 1.0. \end{aligned} \tag{4}$$

Also, the function C_{SS} is given by a third–order polynomial of temperature T (°C), expressed as

$$C_{SS} = 1.9142 \times 10^{-12} + 6.7911 \times 10^{-15}\, T - 1.6638 \times 10^{-17}\, T^2 + 3.9616 \times 10^{-20}\, T^3. \tag{5}$$

Environmental effects on fatigue crack growth of nonirradiated austenitic SSs have been investigated by Shack and Kassner.[70] In the absence of any significant contribution of SCC to growth rate, the CGRs in water with ≈0.3 ppm DO are best represented by the expression

$$\dot{a}_{env} = \dot{a}_{air} + 4.5 \times 10^{-5}\, (\dot{a}_{air})^{0.5}, \tag{6}$$

and in water with ≈8 ppm DO by the expression

$$\dot{a}_{env} = \dot{a}_{air} + 1.5 \times 10^{-4}\, (\dot{a}_{air})^{0.5}. \tag{7}$$

The CGR (m/s) under SCC conditions is represented by the correlation given in the U.S. NRC report NUREG–0313, Rev. 2,[67]

$$\dot{a}_{SCC} = A\, (K)^{2.161}, \tag{8}$$

where K is the stress intensity factor (MPa $m^{1/2}$), and the magnitude of constant A depends on the water chemistry and composition and structure of the steel. A value of 2.1×10^{-13} has been proposed in NUREG–0313 for sensitized SS in water chemistries with 8 ppm DO. The magnitude of constant A will be smaller in low–DO environments, such as HWC BWR or PWR environments.

During crack growth tests in high–temperature water, environmental enhancement of CGRs typically does not occur from the start of the test. Under more rapid cyclic loading, the crack growth is dominated by mechanical fatigue. The CGRs during precracking and initial periods of cyclic loading in these tests were primarily due to mechanical fatigue. For tests under increasing rise times, the crack growth rates first decrease as shown by the curve denoted "Precracking" in Fig. 37, then jump to new, higher, growth rates for loading conditions that would lead to CGRs below 5×10^{-10} m/s in air. For K_{max} values of 15–18 MPa $m^{1/2}$, this means that environmental enhancement occurs for load ratios $R \geq 0.5$ and rise times ≥ 30 s.

After the test the final crack size was marked by fatigue cycling in air at room temperature. The specimens were then fractured, and the fracture surface of both halves of the specimen was photographed with a telephoto lens through the hot cell window. The fracture surfaces of the out–of–cell test specimens

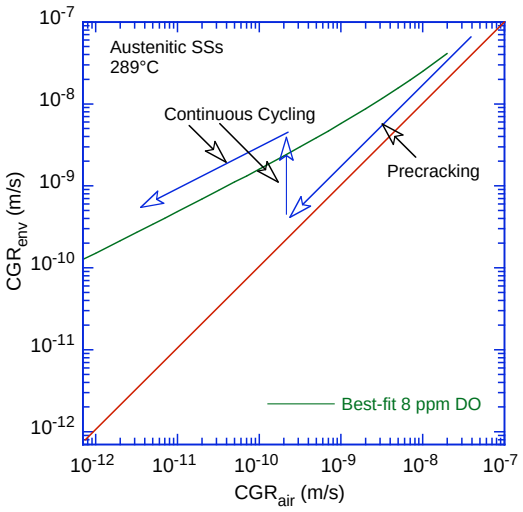

Figure 37.
Plot of CGR in water vs. the CGR in air showing environmental enhancement of growth rates in high purity water at 289°C.

were examined by scanning electron microscopy (SEM). The final crack length of each half of the fractured specimen was determined from the optical or SEM photograph by the 9/8 averaging technique: nine measurements were taken across the width of the specimen at equal intervals, the two near–surface measurements were averaged and the resultant value was averaged with the remaining seven measurements. The results were used to correct the experimental crack length measurements, e.g., the crack extensions determined from the DC potential drop method were proportionately scaled to match the final optically measured crack length.

The CGR test results were validated in accordance with the specimen size criteria of ASTM E–1681 and E–647. These criteria require that the plastic zone at the tip of a fatigue crack be small relative to the specimen geometry. The ASTM specifications for specimen K/size criteria are intended to ensure applicability and transferability of the cracking behavior of a component or specimen of a given thickness under a specific loading condition to a crack associated with a different geometry, thickness, and loading condition. For constant load tests, ASTM E–1681 requires that

$$B_{eff} \text{ and } (W–a) \geq 2.5\ (K/\sigma_{ys})^2, \tag{9}$$

and for cyclic loading ASTM E–647 requires that

$$(W–a) \geq (4/\pi)\ (K/\sigma_{ys})^2, \tag{10}$$

where W is the specimen length, a is the crack length, K is the applied stress intensity factor, and σ_{ys} is the yield stress of the material. The effective thickness B_{eff} of side–grooved specimen is calculated as the root mean square of the full and reduced thicknesses, i.e., $(B \cdot B_N)^{0.5}$. In high–temperature water, because the primary mechanism for crack growth during continuous cycling is not mechanical fatigue, Eq. 9 is the more appropriate criterion, but Eq. 10 may give acceptable results. For high–strain hardening materials, i.e., materials with an ultimate to yield stress ratio $(\sigma_{ult}/\sigma_{ys}) \geq 1.3$, both criteria allow the use of the flow stress defined as $\sigma_f = (\sigma_{ult} + \sigma_{ys})/2$ rather than the yield stress.

The K/size criteria were developed for materials that show work hardening and, therefore, may not be valid for materials irradiated to fluence levels where, on a local level, they do not strain harden. This lack of strain hardening, or strain softening, is most dramatic when dislocation channeling occurs but may also occur at lower fluences. For moderate to highly irradiated material, use of an effective yield stress,

defined as the average of the nonirradiated and irradiated yield stresses, has been suggested;[71] this reduces the irradiation–induced increase in yield stress by one half. In the present study, an effective flow stress was used to determine the valid K_{max} for SS weld HAZ specimens and Heat C3 specimen irradiated to a fluence level of 0.3×10^{21} n/cm^2.

3.2.3 Crack Growth Rates of Irradiated Stainless Steels in BWR Environments

3.2.3.1 Specimen C3–A of Type 304L SS (Heat C3), Test CGRI-12

A crack growth test has been completed on Heat C3 of Type 304L SS irradiated to 0.3×10^{21} n/cm^2. The environmental and loading conditions, experimental CGRs, allowed K_{max} from the K/size criterion in Eq. 9, and the deviation of applied K_{max} from the allowed value are given in Table 7. The test was started in a high–DO environment (≈300 ppb DO in effluent), and the water flow rate was ≈10 mL/min. The ECPs of Pt and SS electrodes in the effluent stream were monitored continuously.

Precracking was carried out at R = 0.3 and K_{max} = 13–14 MPa m$^{1/2}$. After ≈0.3 mm crack advance, R was increased incrementally to 0.7, and the waveform was changed from triangular to saw-tooth with rise times of 12–500 s. The changes in crack length and K_{max} with time during various test periods are shown in Figs. 38. For this specimen, crack growth could not be maintained for loading conditions with high values of R and relatively low K_{max}. For example, at K_{max} = 14 MPa m$^{1/2}$ increasing R from 0.3 to 0.5 essentially stopped crack growth (Fig. 38a). Changing R back to the earlier value did not restore crack growth; K_{max} had to be increased to restart crack growth. To promote environmentally enhanced crack growth, the rise time for the cyclic loading at R = 0.3 was increased from 0.5 to 300 s before increasing R (Fig. 38b). For R = 0.7, crack growth occurred only at K_{max} greater than 17 MPa m$^{1/2}$.

Table 7. Crack growth results for Specimen C3–A of Type 304 SS[a] in high–purity water at 289°C.

Test Period	Test Time, h	ECP[b] mV (SHE) Pt	ECP[b] mV (SHE) Steel	O_2 Conc.,[b] ppb	Load Ratio	Rise Time, s	Down Time, s	Hold Time, s	K_{max}, MPa·m$^{1/2}$	ΔK, MPa·m$^{1/2}$	Growth Rate, m/s	K_{max} from Eq. 13, MPa m$^{1/2}$	Deviation in K_{max}, %
Pre	55	226	167	300	0.31	0.5	0.5	0	12.9	8.9	2.94E-09	18.4	-30
1	165	212	166	300	0.30	0.5	0.5	0	14.0	9.8	8.37E-09	17.9	-22
2a	189	221	169	300	0.50	5	5	0	13.9	6.9	negligible	17.9	-23
2b	193	211	169	300	0.50	0.5	0.5	0	13.8	6.9	negligible	17.9	-23
2c	214	209	161	300	0.30	0.5	0.5	0	13.9	9.7	negligible	17.9	-23
2d	219	211	163	300	0.30	0.5	0.5	0	15.0	10.5	1.48E-08	17.7	-15
3	364	218	171	300	0.30	1	1	0	15.9	11.1	1.39E-08	17.5	-9
4	380	218	171	300	0.30	30	4	0	16.0	11.2	1.33E-09	17.4	-8
5	404	219	177	300	0.29	300	4	0	15.9	11.3	3.29E-10	17.4	-8
6	479	204	173	300	0.48	300	4	0	15.7	8.2	4.75E-11	17.4	-10
7	596	235	187	300	0.70	12	12	0	15.7	4.7	negligible	17.4	-10
8	670	228	188	300	0.70	12	12	0	17.6	5.3	6.23E-11	17.3	2
9	717	231	186	300	0.70	12	12	3600	17.8	–	–	17.3	3
10	910	234	197	300	0.70	500	12	3600	17.9	–	8.65E-11	17.2	4
11	1080	232	200	300	0.70	500	12	3600	22.0	–	1.11E-10	17.1	29
12	1175	226	203	300	0.70	500	1	9500	22.3	–	1.28E-10	17.0	31

[a] Heat C3, irradiated to 0.3×10^{21} n/cm^2.
[b] Represents values in the effluent. Conductivity was 0.07 and 0.3–0.45 μS/cm in feedwater and effluent, respectively. Feedwater pH at room temperature was 6.5.

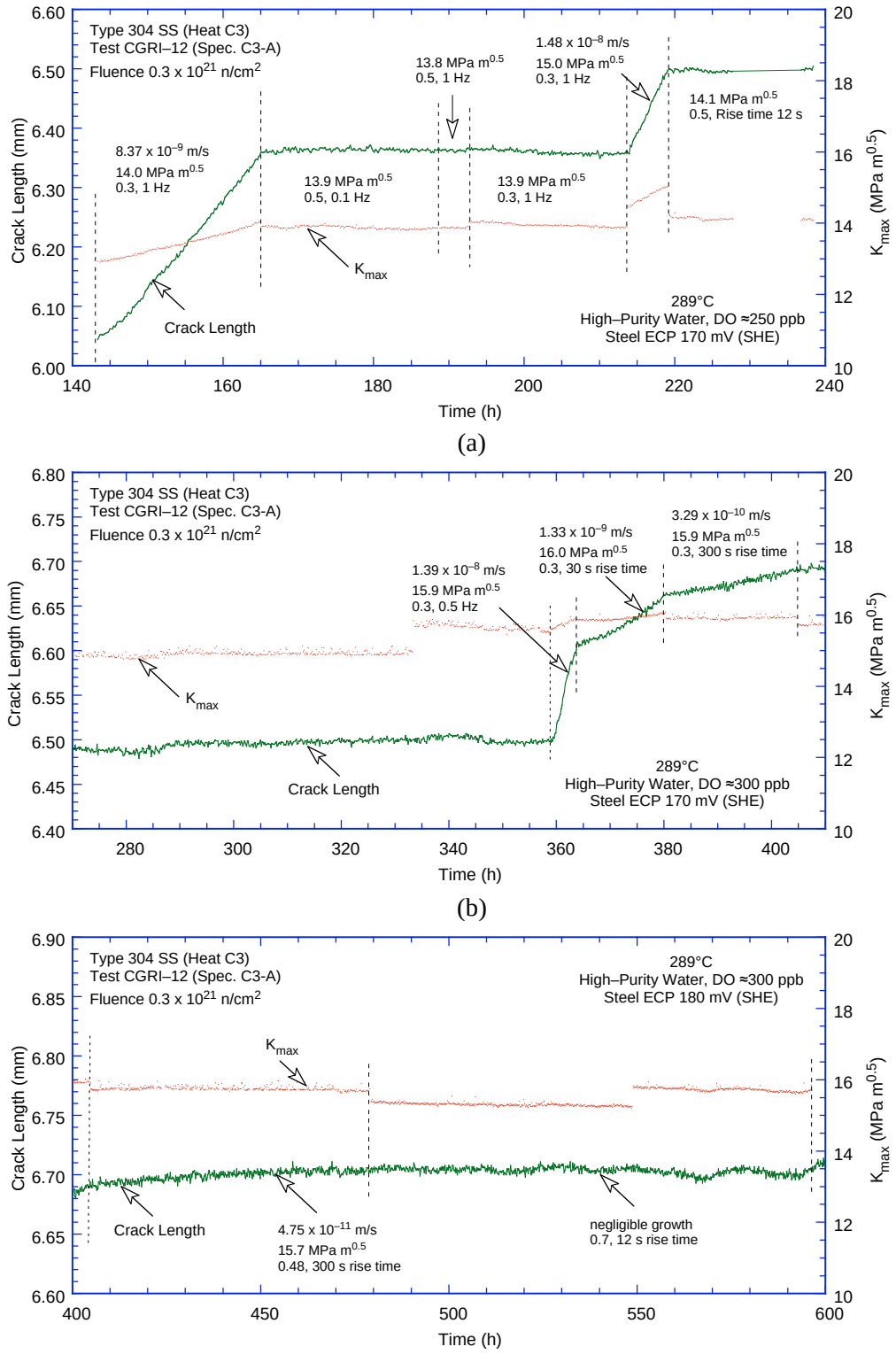

Figure 38. Crack length vs. time plots for irradiated Type 316 SS (Heat C16) in high–purity water at 289°C during test periods (a) 1–2, (b) 3–5, (c) 6–7, (d) 8–10, and (e) 11–12.

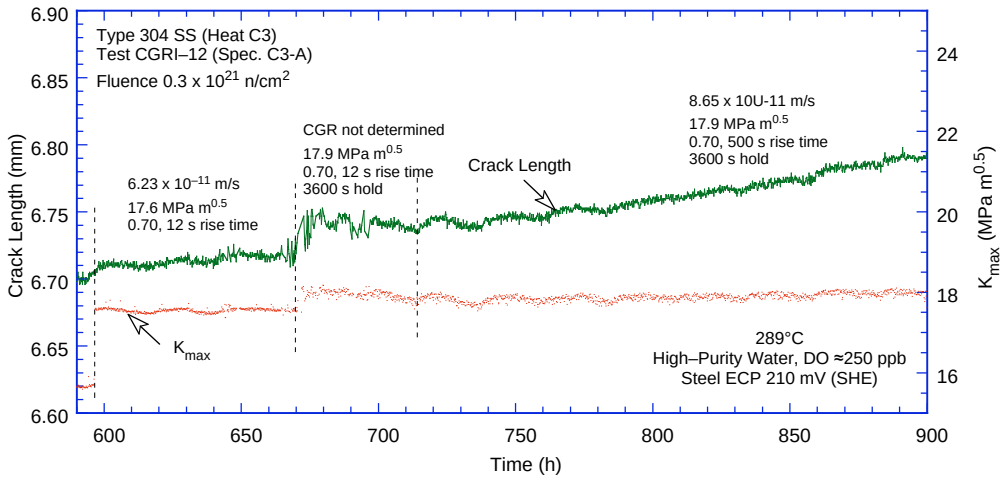

(d)

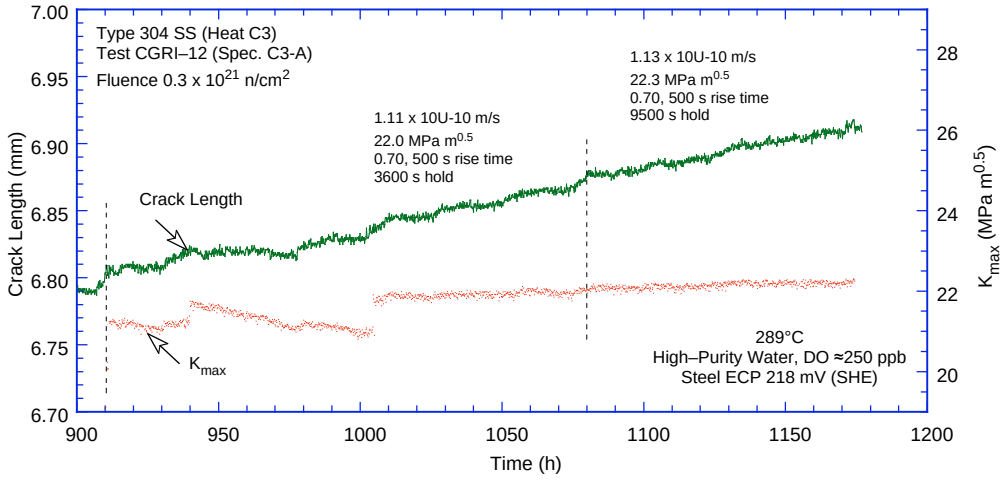

(e)

Figure 38. (Cont'd)

Crack growth rates could not be measured during test period 9 because of significant variations in the autoclave temperature, which resulted in large fluctuations in the DC potential measurements (Fig. 38d). Also, during test period 11 (Fig. 38e), applied K_{max} gradually decreased from the desired value of 22 to 20.5 MPa $m^{1/2}$ over a 50–h period because of a faulty back–pressure regulator. Specimen C3–A irradiated to 0.3 x 10^{21} n/cm^2 showed very little environmental enhancement of CGRs both under continuous cycling and SCC conditions. There was no change in CGR when the hold time was increased from 3600 to 9500 s (Fig. 38e, test periods 11 and 12).

A photomicrograph of the fracture surface of both halves of the test specimen is shown in Fig. 39. The final crack length, determined from the photograph, showed very good agreement with the value estimated from the DC potential measurement. Also, the results in Table 7 indicate that for specimen C3–A, loading conditions for all test periods, except 11 and 12, satisfied the K/size criterion of Eq. 9.

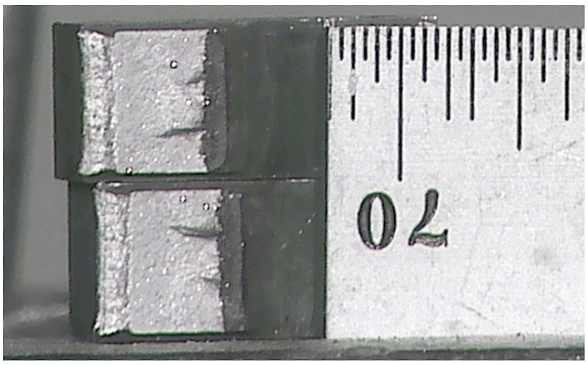

Figure 39.
Photomicrograph of the fracture surface of Specimen C3–A.

3.2.3.2 Irradiated Austenitic SSs under Continuous Cycling

For continuous cyclic loading, the experimental CGRs for specimen C3-A and other specimens of irradiated Heats C3 and C16 in BWR environments are compared in Fig. 40 with the CGRs predicted for austenitic SSs in air under the same loading conditions. The curves in the figure are calculated from the Shack/Kassner model for nonirradiated austenitic SSs in high–purity water with either 8 or 0.2 ppm DO (Eqs. 6 and 7, respectively) and are included to provide a comparison with the irradiated CGR data.

The results for SSs irradiated to 0.9 or 2.0 x 10^{21} n/cm^2 (1.35 or 3.0 dpa) indicate significant enhancement of the CGRs in high–DO water under cyclic loading with long rise times. The CGRs for Heat C3 irradiated to either 0.9 or 2.0 x 10^{21} n/cm^2 (open circles and triangles) and for Heat C16 irradiated to 2.0 x 10^{21} n/cm^2 (solid triangles) are comparable. For these irradiation conditions, the CGRs in water with ≈ 300 ppb DO are slightly higher than the rates predicted by the Shack/Kassner model for nonirradiated austenitic SSs in high–purity water with 8 ppm DO (Fig. 40a).

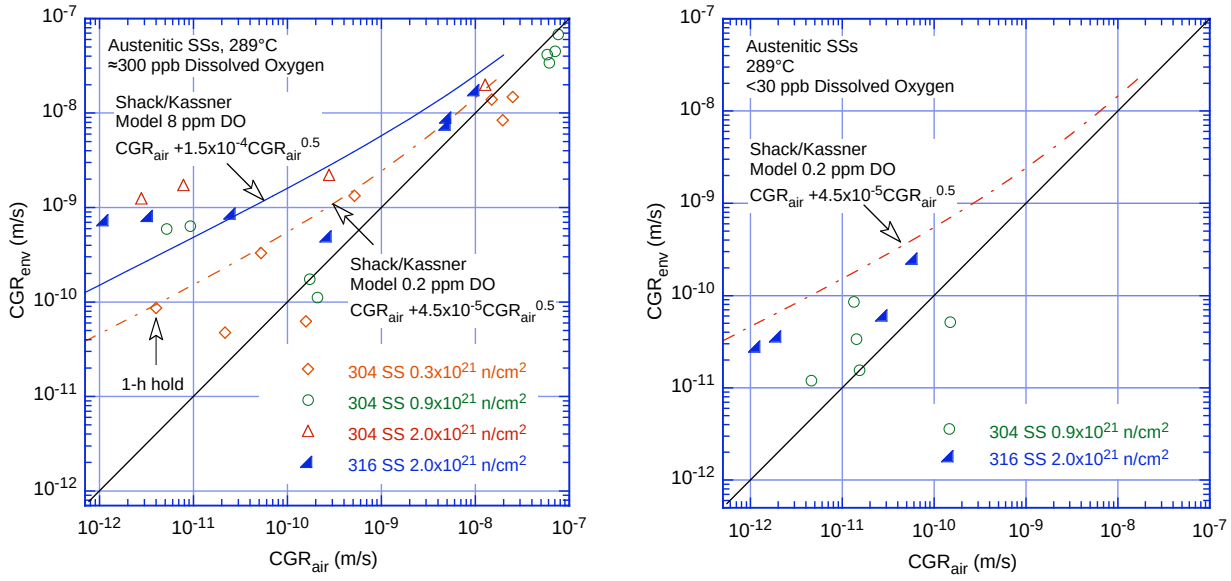

(a) (b)

Figure 40. CGR data for irradiated austenitic SSs under continuous cycling at 289°C in high–purity water with (a) ≈300 ppb and (b) <30 ppb dissolved oxygen.

Heat C3 irradiated to 0.3 x 10^{21} n/cm^2 (0.45 dpa) shows less environmental enhancement of CGRs in high–DO water (open diamonds in Fig. 40a); the CGRs in water with ≈ 300 ppb DO are best represented by the Shack/Kassner model for nonirradiated austenitic SSs in high–purity water with 0.2 ppm DO.

For continuous cyclic loading, decreasing the DO level has a beneficial effect on CGRs, e.g., decreasing the DO from ≈300 ppb DO to <30 ppb DO results in a factor of 25 decrease in the CGR. The growth rates are slightly lower for the irradiated steels in water with <30 ppb DO than for nonirradiated austenitic SSs in high–purity water with 0.2 ppm DO (Fig. 40b). The CGR data in the low–DO environment were not obtained for specimen C3-A because the relatively low CGRs expected for the material would have required long test durations. Based on other test results, the benefit of reduced DO is expected for Heat C3 irradiated to 0.3 x 10^{21} n/cm^2. The CGR data in low–DO environment was also not obtained for specimen C3–C irradiated to 2 x 10^{21} n/cm^2.

3.2.3.3 CGRs of Irradiated Austenitic SSs under Trapezoidal Waveform with Long Hold Periods

The experimental CGRs for irradiated Heats C3 and C16 obtained with a trapezoidal waveform (i.e., constant load with periodic partial unloading) in high– and low–DO water are plotted in Fig. 41. In high–DO water, the CGRs of Types 304L and 316L SS (Heats C3 and C16) irradiated to either 0.9 or 2.0 x 10^{21} n/cm^2 are a factor of ≈5 higher than the disposition curve for sensitized SSs in water with 8 ppm DO given in NUREG–0313.[67] The growth rates for the two steels at the same fluence level, as well as those for Heat C3 irradiated to 0.9 and 2.0 x 10^{21} n/cm^2 fluence levels, are comparable. In high–DO water, the CGRs for Type 304L Heat C3 irradiated to 0.3 x 10^{21} n/cm^2 are below the disposition curve for sensitized SSs in water with 8 ppm DO given in NUREG–0313.

The results also indicate a benefit from a low–DO environment. For Heat C3 irradiated to 0.9 x 10^{21} n/cm^2 and Heat C16 irradiated to 2.0 x 10^{21} n/cm^2 (circles and right triangles in Fig. 41), the CGRs decreased more than an order of magnitude when the DO level was decreased from ≈300 to <30 ppb. No benefit of low–DO environment was observed for Heat C3 irradiated to 2.0 x 10^{21} n/cm^2 (solid isosceles triangles in Fig. 41). However, the applied K_{max} for the test period in low–DO water was

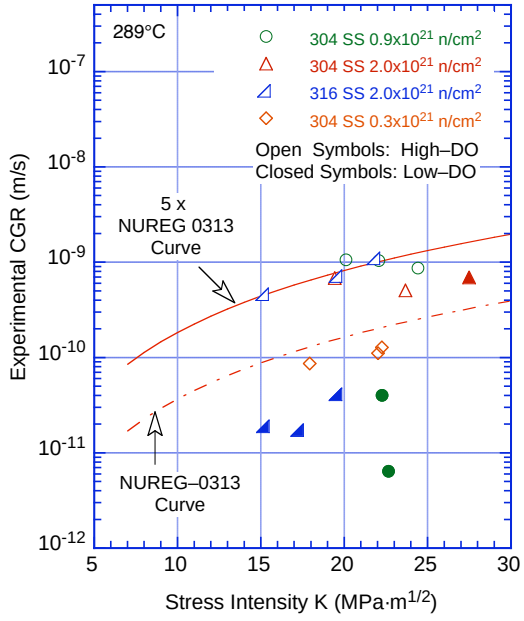

Figure 41.
CGR data under constant load with periodic partial unloads for irradiated austenitic SSs in high–purity water at 289°C.

44% greater than the allowable value based on the K/size criterion in Eq. 9. A detailed metallographic examination of the fracture surface of the specimen will be performed to validate the test results.

3.2.4 Crack Growth Tests on Nonirradiated Stainless Steel Weld HAZ Specimens

This section presents the results of crack growth tests in the BWR environment on nonirradiated 1/4–T CT specimens of Type 304L GG core shroud H5 weld HAZ and Type 304 laboratory–prepared weld HAZ. The GG weld HAZ specimens were from the bottom shell of the H5 weld and were in the as–welded condition (GG5B–A) and the as–welded plus thermally treated condition (GG3B–A–TT). The Type 304 SS laboratory prepared weld HAZ specimen was in the as–welded plus thermally treated condition (853B–A–TT).

3.2.4.1 Specimen GG5B–A of the HAZ from Grand Gulf Core Shroud H5 SA Weld, Test CGR–10

The environmental and loading conditions, experimental CGRs, allowed values of K_{max} from the K/size criterion, and the deviation of applied K_{max} from the allowed value are given in Table 8. The changes in the crack length and K_{max} with time during the various test periods are shown in Fig. 39. The test was started in high–DO water (≈580 ppb DO in effluent) and a flow rate of 140 mL/min. Because of a faulty reference electrode, the ECPs of the Pt and SS electrodes in the effluent could not be monitored during the test. The water conductivity was monitored continuously.

Precracking was initiated at R = 0.23, K_{max} ≈15 MPa $m^{1/2}$, and a triangular waveform. After ≈0.6 mm crack advance, R was increased incrementally to 0.7, and the waveform changed to a slow/fast sawtooth with a rise time of 30 s; in all cases the fast rate (time to unload) was 2 s. During the initial 300–h test period (i.e., precracking and test periods 1–2b in Table 8), no environmental enhancement was observed in the measured growth rates. Also, decreasing the flow rate from 140 to 35 mL/min had little or no effect on the CGRs, although the conductivity increased from 0.08 to 0.12 μS/cm.

Table 8. Crack growth results for Specimen GG5B–A[a] of Type 304L HAZ in high–purity water at 289°C.

Test Period[b]	Test Time, h	Flow Rate, cc/min	Cond.,[c] μS/cm	O_2 Conc.,[c] ppb	R Load Ratio	Rise Time, s	Down Time, s	Hold Time, s	K_{max}, MPa·$m^{1/2}$	ΔK, MPa·$m^{1/2}$	Growth Rate, m/s	Allowed K_{max},[d] MPa·$m^{1/2}$	Deviation in K_{max},[d] %
Pre a	97	140	0.07	580	0.23	0.25	0.25	0	16.7	12.9	7.57E-08	19.3	-13
Pre b	98	140	0.07	580	0.23	0.25	0.25	0	15.0	11.5	3.42E-08	19.1	-22
Pre c	114	140	0.08	590	0.23	7.5	7.5	0	14.2	11.0	3.59E-10	19.1	-25
Pre d	120	140	0.07	590	0.23	0.50	0.50	0	15.7	12.1	3.40E-08	18.7	-16
1	143	140	0.08	485	0.52	30	2	0	15.5	7.4	5.85E-11	18.6	-17
2a	259	30	0.12	440	0.71	30	2	0	17.0	4.9	negligible	18.6	-9
2b	306	35	0.14	450	0.71	30	2	0	17.0	4.9	1.52E-11	18.6	-9
2c*	337	35	0.14	464	0.72	30	2	0	20.6	5.8	3.15E-10	18.6	11
3*	407	35	0.14	460	0.71	300	2	0	20.8	6.0	1.81E-10	18.5	13
4*	455	35	0.13	500	0.71	1,000	2	0	20.9	6.1	1.26E-10	18.5	13
5	572	35	0.13	500	0.71	12	12	3600	21.1	–	6.01E-11	18.4	14
6	646	105	0.08	500	0.71	12	12	3600	26.5	–	1.72E-10	18.3	45
7	692	105	0.07	500	0.71	12	12	3600	26.9	–	1.55E-10	18.2	47
8	767	105	0.07	500	0.71	1,000	2	0	27.4	7.9	3.18E-10	18.1	51

[a]Nonirradiated Grand Gulf H5 SA weld bottom shell HAZ, as–welded condition.
[b]An asterisk indicates environmental enhancement of growth rates under cyclic loading.
[c]Represents values in the effluent.
[d]Based on flow stress.

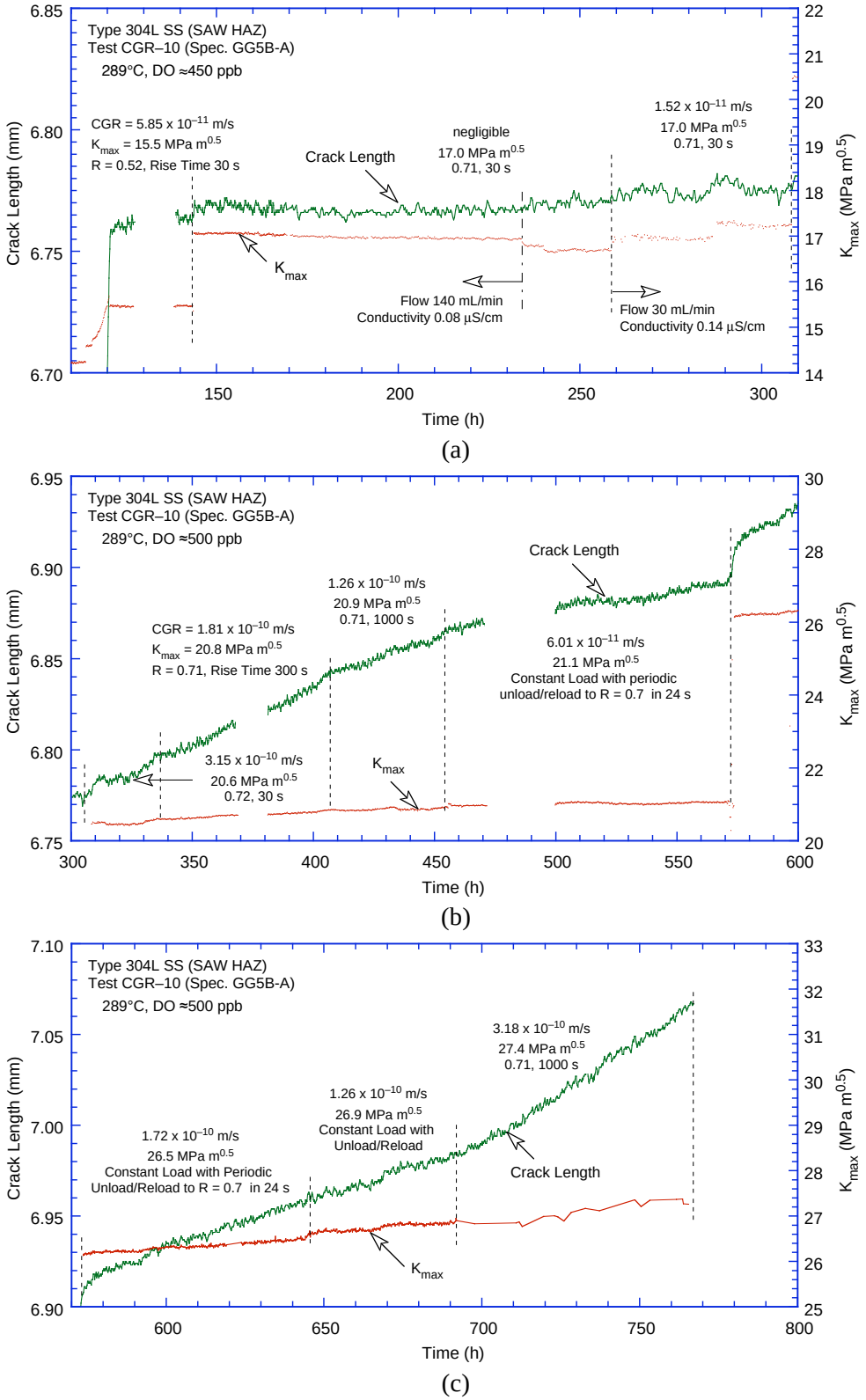

Figure 42. Crack length vs. time plots for nonirradiated HAZ specimen of Grand Gulf Type 304L bottom shell H5 weld in high–purity water at 289°C during test periods (a) precracking–3, (b) 4-6, and (c) 7–8.

After ≈310 h, K_{max} was increased to ≈20 MPa $m^{1/2}$, and the rise time was increased to 300 s and then 1000 s. Under these conditions, environmental enhancement of CGRs occurred. After ≈450 h the loading waveform was changed to trapezoidal waveform with 3600 s hold period and 12–s unload and reload periods. For Specimen GG5B–A, the experimental K_{max} values were generally higher (≈13% higher during test periods 2c–5 and over 45–50% higher during periods 6–8) than the allowed K_{max} based on flow stress and Eq. 9.

Photomicrographs of the fracture surface of the two halves of the broken specimen are shown in Fig. 43. A relatively straight crack front is evident. The crack lengths were measured by both optical and scanning electron microscopy. The results showed very good agreement with the values estimated from the DC potential measurements; the difference in measured and estimated values was <5%.

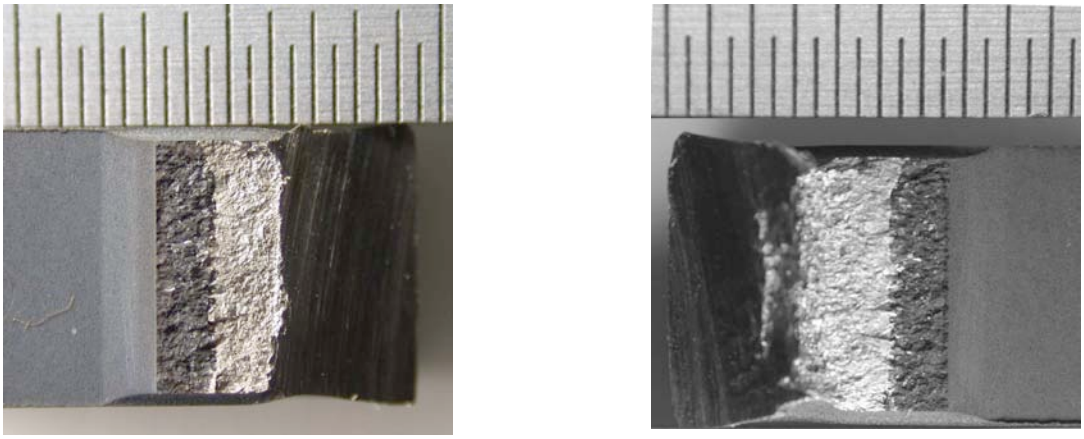

(a) (b)

Figure 43. Photomicrograph of the fracture surface of Specimen GG5B–A.

After the test both halves of the fractured specimen were then cleaned chemically to remove the surface oxide film, and the fracture surface was examined by SEM. A micrograph of the fracture surface for Specimen GG5B–A is shown in Fig 44. Micrographs showing a slice of the entire crack advance during the test and typical fracture morphology at select locations on the surface are given in Fig. 45. With minor variations, a predominantly transgranular (TG) fracture morphology appears for the entire test. Most of the TG facets show a well–defined river pattern (Fig 45a). Also, a TG fracture with river pattern is observed from room–temperature cycling after the test (Fig. 45d) to mark the final crack front.

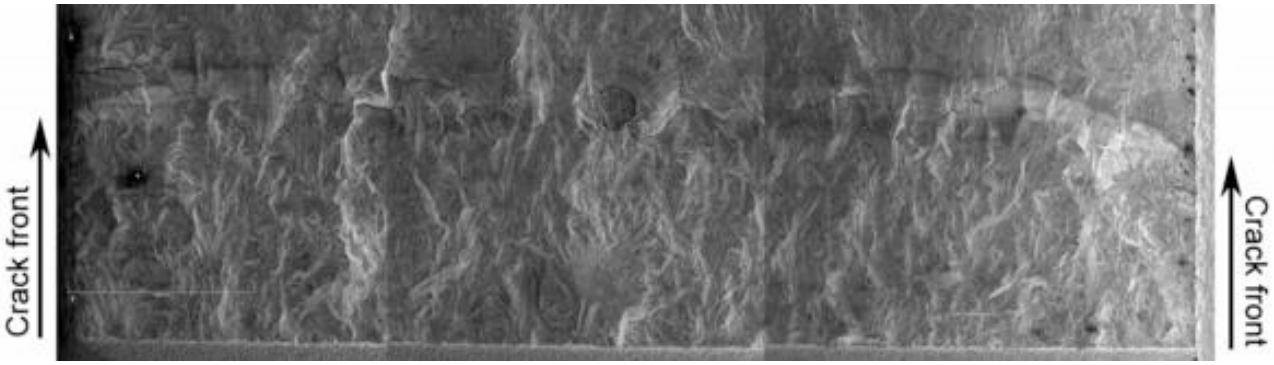

Figure 44. Micrograph of the fracture surface of Specimen GG5B–A tested in high–DO water at 289°C.

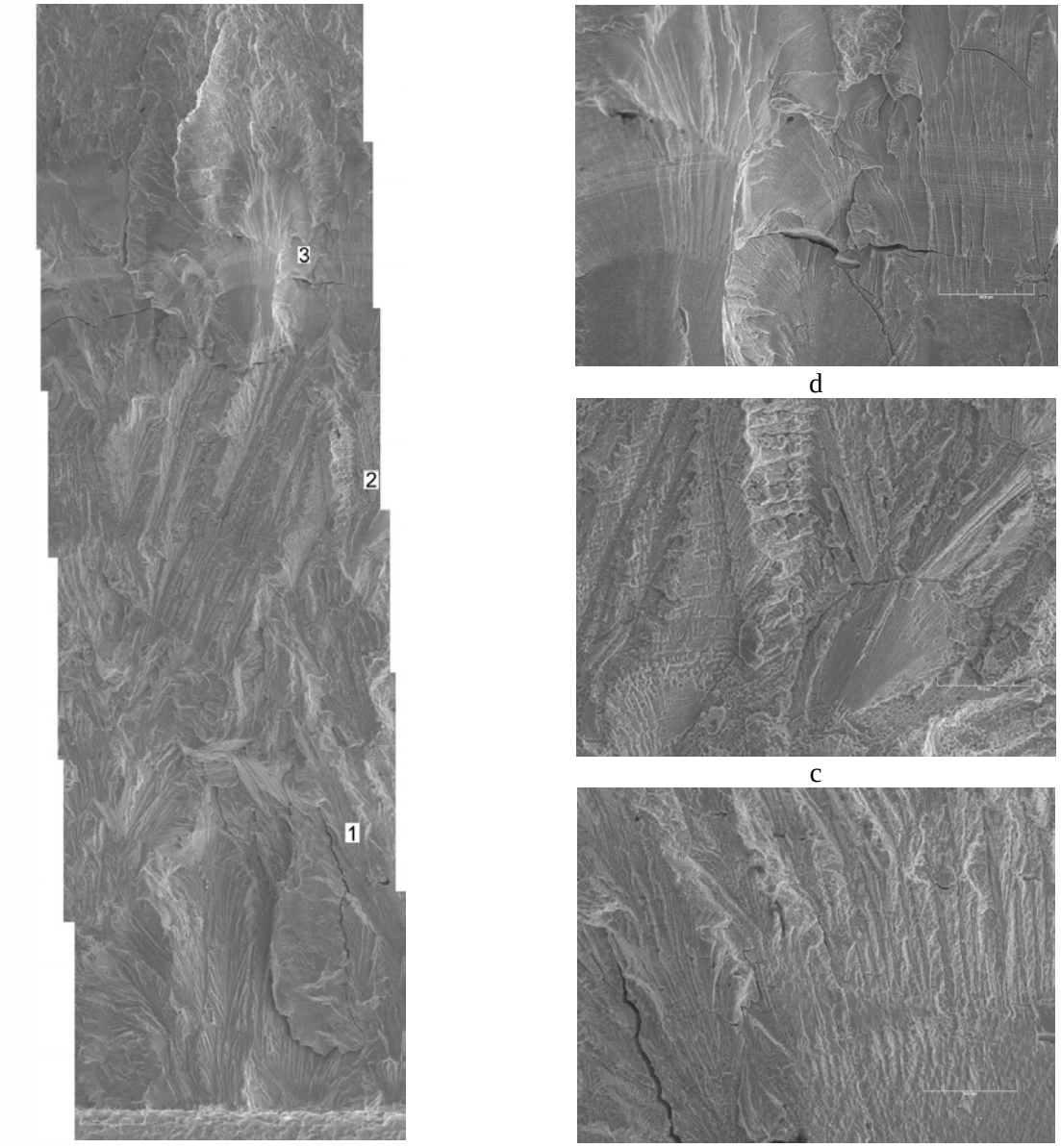

Figure 45. Micrographs showing (a) slice of the entire length of fracture surface, and (b), (c), and (d) high magnification micrographs of the fracture surface at locations 1, 2, and 3, respectively.

3.2.4.2 Specimen 85–3A–TT of the HAZ from Laboratory–Prepared SMA Weld, Test CGR-11

The environmental and loading conditions, experimental CGRs, allowed values of K_{max} from the K/size criterion, and deviation of applied K_{max} from the allowed value are given in Table 9. The test was started in a high–DO environment (e.g., effluent DO level of ≈600 ppb); the water flow rate was maintained constant at ≈105 mL/min during the test. The effluent water conductivity and ECPs of a Pt and SS electrode were monitored continuously; the values are listed in the table. The effluent DO level was measured periodically.

Table 9. Crack growth results for Specimen 85–3A–TT[a] of nonirradiated Type 304 SS SMA weld HAZ in high–purity water at 289°C.

Test Period[b]	Test Time, h	Cond.,[c] µS/cm	ECP[c] mV (SHE) Pt	ECP[c] mV (SHE) Steel	R Load Ratio	Rise Time, s	Down Time, s	Hold Time, s	K_{max}, MPa·m$^{1/2}$	ΔK, MPa·m$^{1/2}$	Growth Rate, m/s	Allowed K_{max}, MPa m$^{1/2}$	Deviation in K_{max},[d] %
Pre a	144	0.10	183	27	0.21	0.50	0.50	0	16.13	12.74	5.46E-08	15.7	3
Pre b	148	0.08	182	32	0.21	0.50	0.50	0	15.01	11.86	5.00E-08	15.4	-2
1	166	0.07	182	32	0.51	30	2	0	14.64	7.18	5.61E-11	15.3	-5
2	190	0.07	184	41	0.51	30	2	0	16.73	8.20	5.50E-10	15.3	9
3	215	0.07	182	45	0.71	30	2	0	16.90	4.90	3.16E-11	15.3	11
4*	264	0.07	184	60	0.71	30	2	0	19.82	5.75	8.85E-10	15.1	32
5a*	298	0.07	188	68	0.71	300	2	0	19.80	5.74	2.75E-10	15.0	32
5b*	338	0.07	187	79	0.71	300	2	0	20.24	5.87	7.91E-10	14.8	36
6*	384	0.07	188	87	0.70	1000	2	0	20.51	6.15	4.57E-10	14.7	39
7	478	0.07	192	106	0.70	12	12	3600	21.15	0.00	6.60E-10	14.4	47
8	646	0.14	-482	-633	0.70	12	12	3600	21.37	0.00	9.13E-11	14.3	49
9	862	0.12	-477	-621	0.70	12	12	3600	24.96	0.00	4.29E-11	14.2	76

[a]Grand Gulf H5 SA weld bottom shell HAZ, nonirradiated.
[b]An asterisk indicates environmental enhancement of growth rates under cyclic loading.
[c]Represents values in the effluent. Water flow rate was maintained at ≈105 mL/min; the DO level in the effluent was ≈600 ppb during the high–DO test and <40 ppb during the low–DO test.
[d]Based on flow stress.

Precracking was initiated at R ≈0.2, K_{max} ≈14 MPa m$^{1/2}$, and a triangular waveform. After ≈0.4 mm crack advance, R was increased incrementally to 0.7, and the waveform was changed to a slow/fast sawtooth with rise times of 30–1000 s; in all cases time to unload was 2 s. The constant load tests were conducted using a trapezoidal waveform with R = 0.7, 1–h hold period at peak load, and 12–s unload and reload periods. During each test period, the maximum stress intensity factor was maintained approximately constant by periodic load shedding (less than 2% decrease in load at any given time).

After ≈480 h, the DO level in the feedwater was decreased from ≈600 ppb to <40 ppb by sparging the feedwater tank with pure N_2. Changes in crack length and ECP of Pt and SS electrodes during the transient period are shown in Fig. 46. For this test, because the flow rate was higher than the rate used for the in–cell tests, changes in the environment were significantly faster. However, the changes in the steel ECP were slower compared with the Pt ECP, e.g., the ECP decreased below –400 mV (SHE) within 10 h

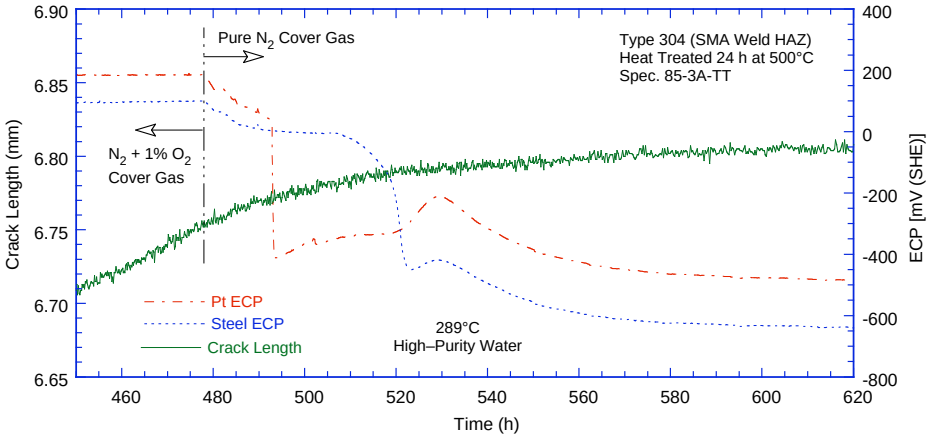

Figure 46. Change in crack length and ECP of Pt and SS electrodes during test periods 5–6 and the intermediate transition period.

for the Pt electrode and 40 h for the steel electrode. A slight increase in ECP values of both Pt and steel electrode at ≈530 h was associated with an increase in the effluent DO level.

After the test, the final crack front was marked by fatigue cycling in air at room temperature. A detailed metallographic evaluation of the specimen was performed to examine the fracture surface and fracture plane morphologies. A 1–mm–thick slice of the entire CT specimen was cut off, and the remainder of the specimen was pulled apart. Photomicrographs of the fracture surface of the two halves of the broken specimen are shown in Fig. 47, and a composite micrograph of the cross section of the specimen is shown in Fig. 48. The crack lengths were measured by both optical and scanning–electron microscopy. The actual final crack extension was ≈40% greater than the value determined from the DC potential measurements. Crack extensions estimated from the DC potential drop method were scaled proportionately; the corrected values of K_{max} and growth rates are listed in Table. 9.

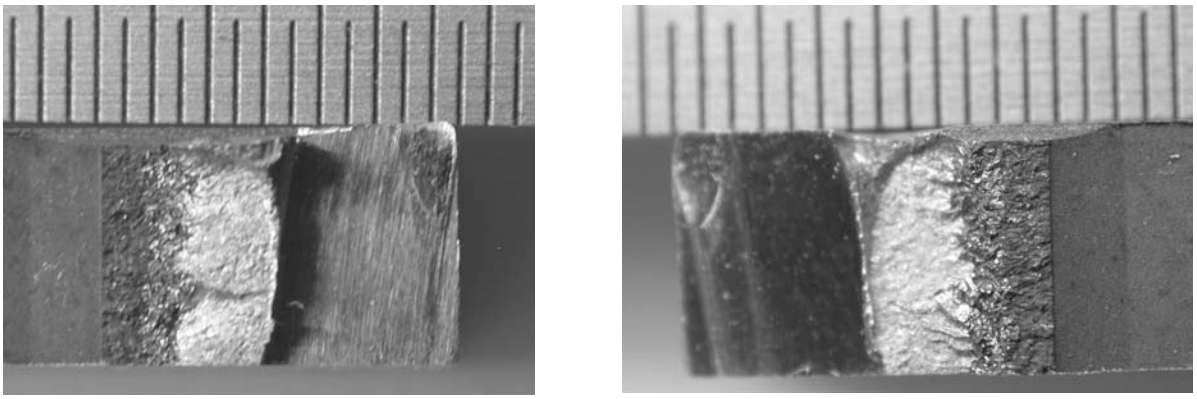

(a) (b)

Figure 47. Photomicrographs of the fracture surfaces of the two halves of Specimen 85–3A-TT.

The changes in crack length and K_{max} with time during the test periods are shown in Fig. 49. For this specimen, significant environmental enhancement occurred after ≈210 h when K_{max} was increased from ≈17 to 20 MPa $m^{1/2}$ (Fig. 49b). Also, the results in Table 9 indicate that the loading conditions from precracking up to test period 3 satisfy the K/size criterion and are ≈34% higher than the allowed value for periods 4–6, 48% higher for period 7 and 8, and 76% higher for period 9.

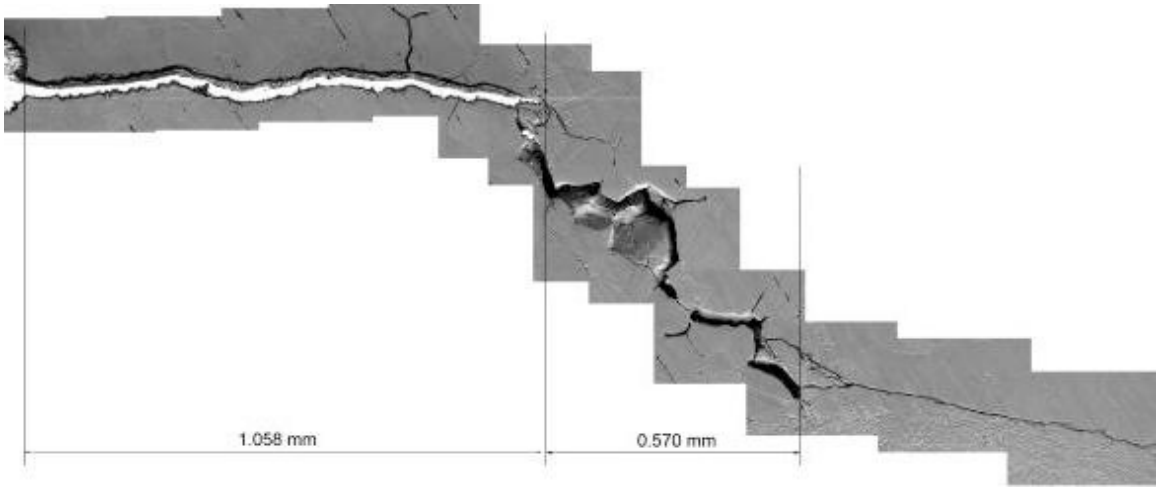

Figure 48. Micrograph of the cross section of Specimen 85-3A-TT showing the fracture plane profile.

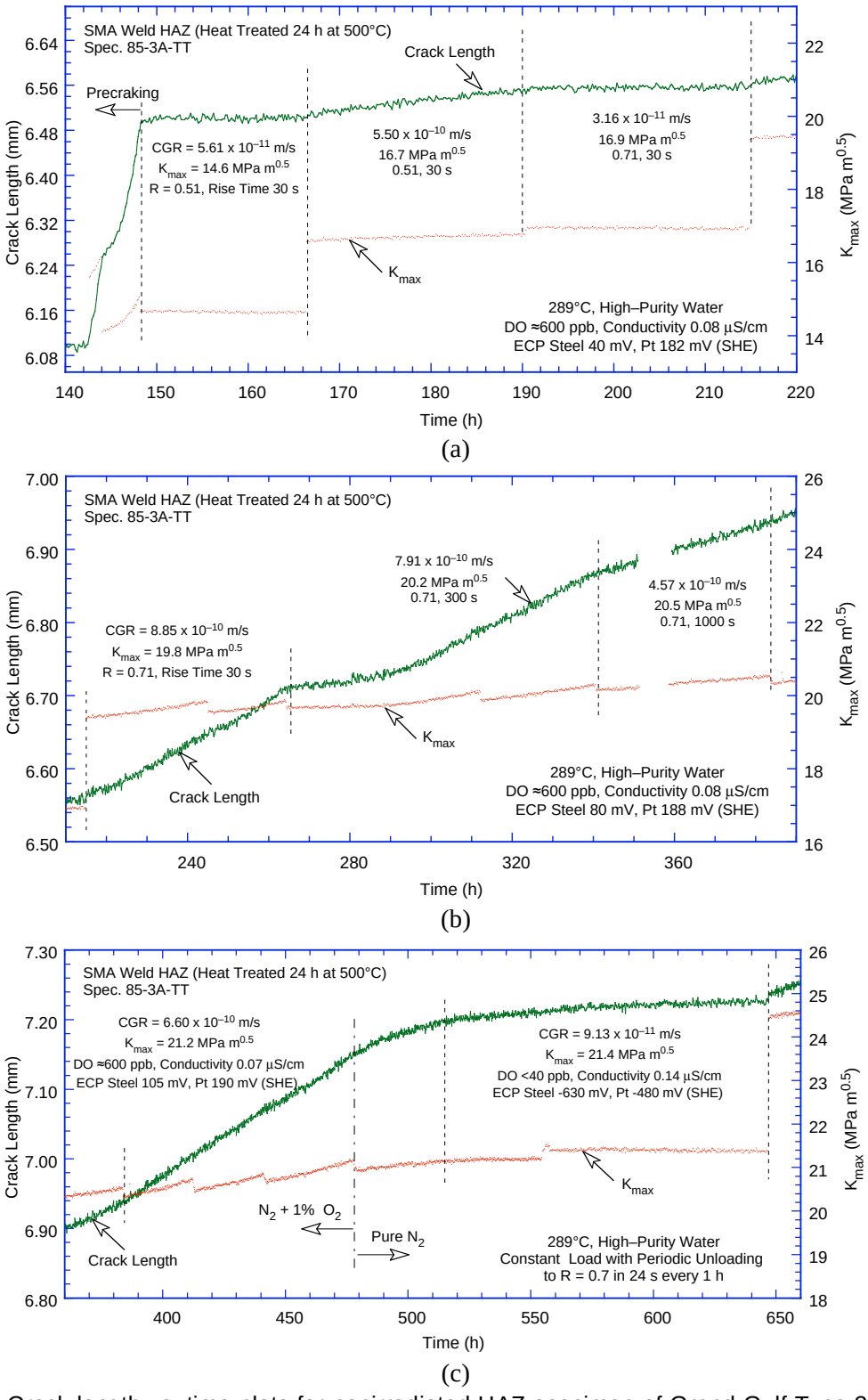

Figure 49. Crack length vs. time plots for nonirradiated HAZ specimen of Grand Gulf Type 304L bottom shell H5 weld HAZ in high–purity water at 289°C during test periods (a) 1–3, (b) 4-6, (c) 7–8, and (d) 9.

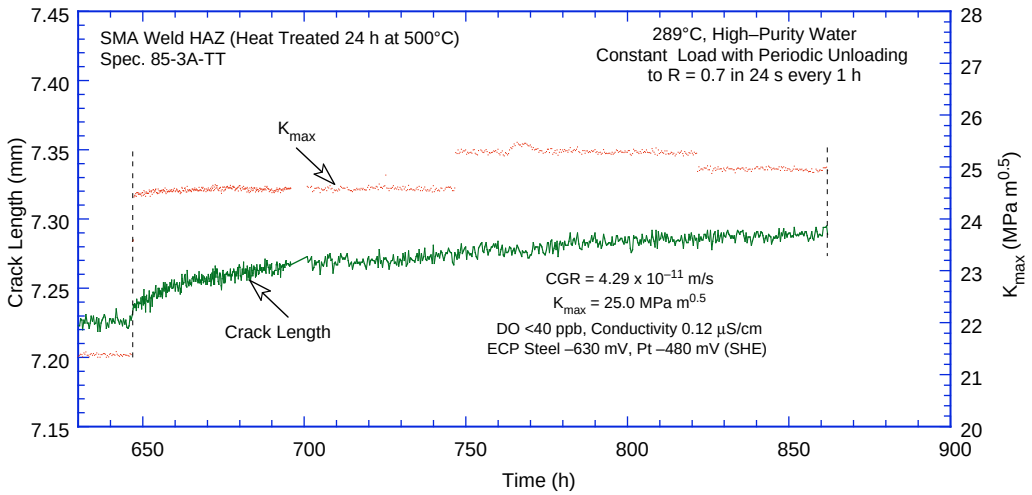

(d)

Figure 49. (Contd.)

The fracture plane orientation shown in Fig. 48 suggests that the applied K_{max} during the last few test periods may have exceeded the K/size criterion. The fracture plane is initially normal to the stress axis, but for the last ≈0.6 mm crack extension it is at 45° to the stress axis. The change in the fracture plane orientation occurred at an average crack extension of 1.16 mm; actual values varied ≈1.0–1.25 mm across the thickness of the specimen. Also, the fracture surface morphology is predominantly TG along the plane normal to the stress axis and completely IG along the plane 45° to the stress axis. A micrograph of the fracture surface for Specimen 85–3A-TT is shown in Fig 50.

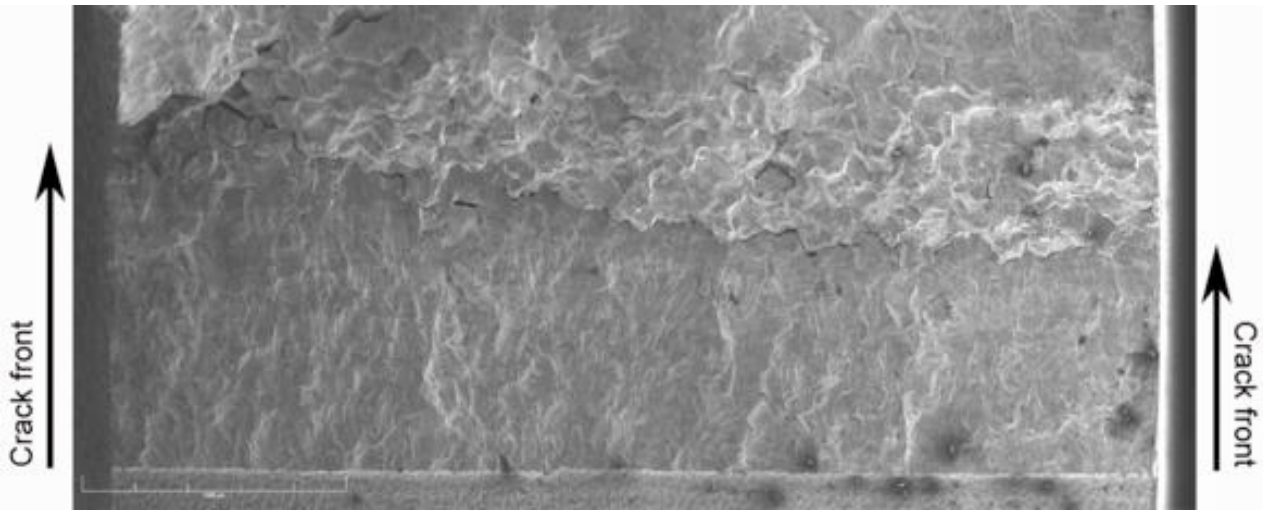

Figure 50. Micrograph of the fracture surface of Specimen 85-3A-TT tested in high–DO water at 289°C.

Micrographs showing a slice of the fracture surface that was normal to the stress axis and the typical fracture morphology at select locations on the surface are given in Fig. 51. The specimen was cleaned chemically to remove the surface oxide film. The fracture surface that is normal to the stress axis exhibits a predominantly TG fracture morphology, and most of the TG facets show a well–defined river pattern (Fig. 51c, d). A narrow region of IG fracture is observed before the fracture plane orientation changed along the plane 45° to the stress axis. Typical fracture morphologies along the change in the fracture plane orientation and before and after the change are shown in Fig. 52.

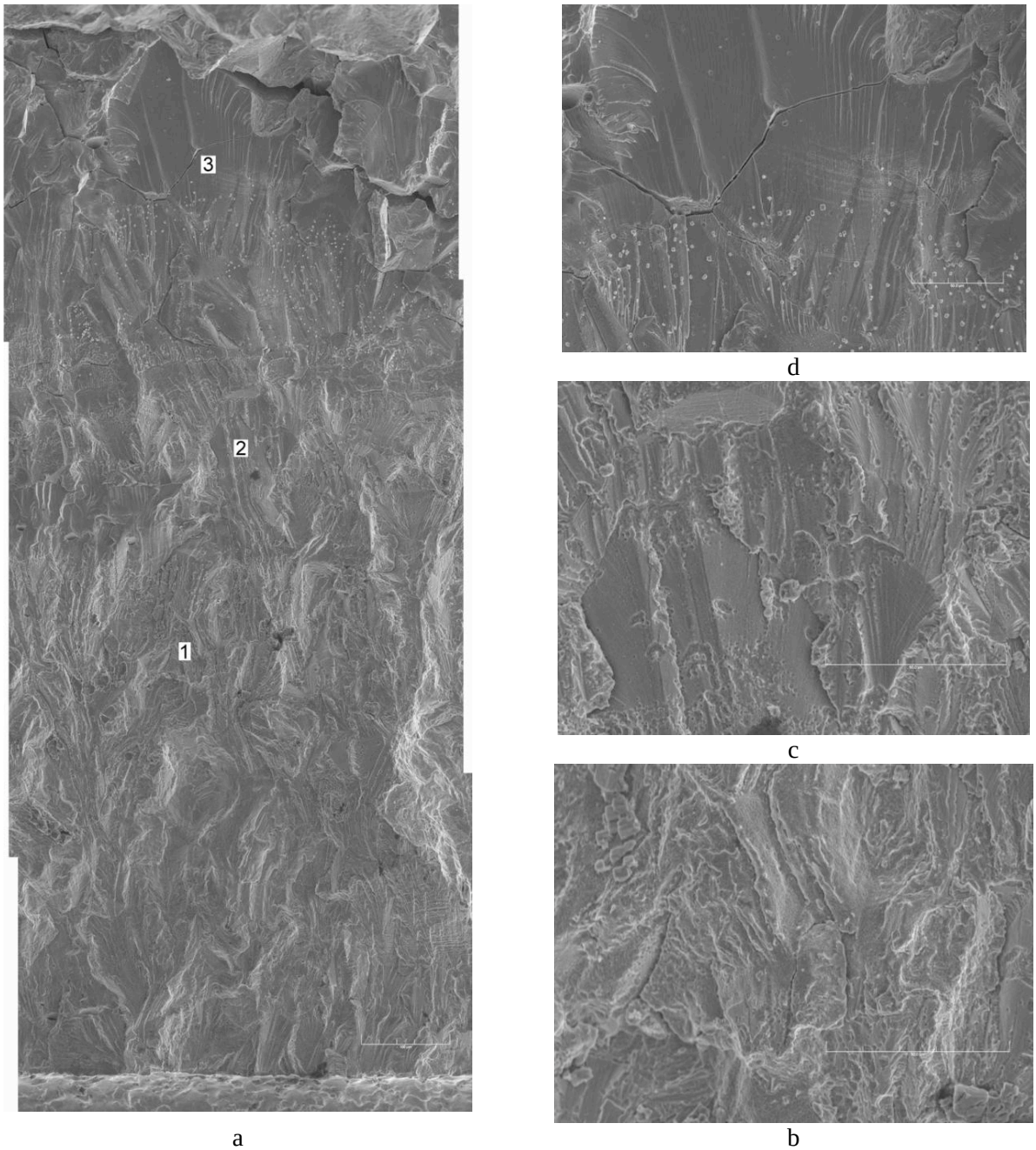

Figure 51. Micrograph showing (a) slice of the fracture surface that was perpendicular to the stress axis, and (b), (c), and (d) high-magnification micrographs of the fracture surface at locations 1, 2, and 3, respectively.

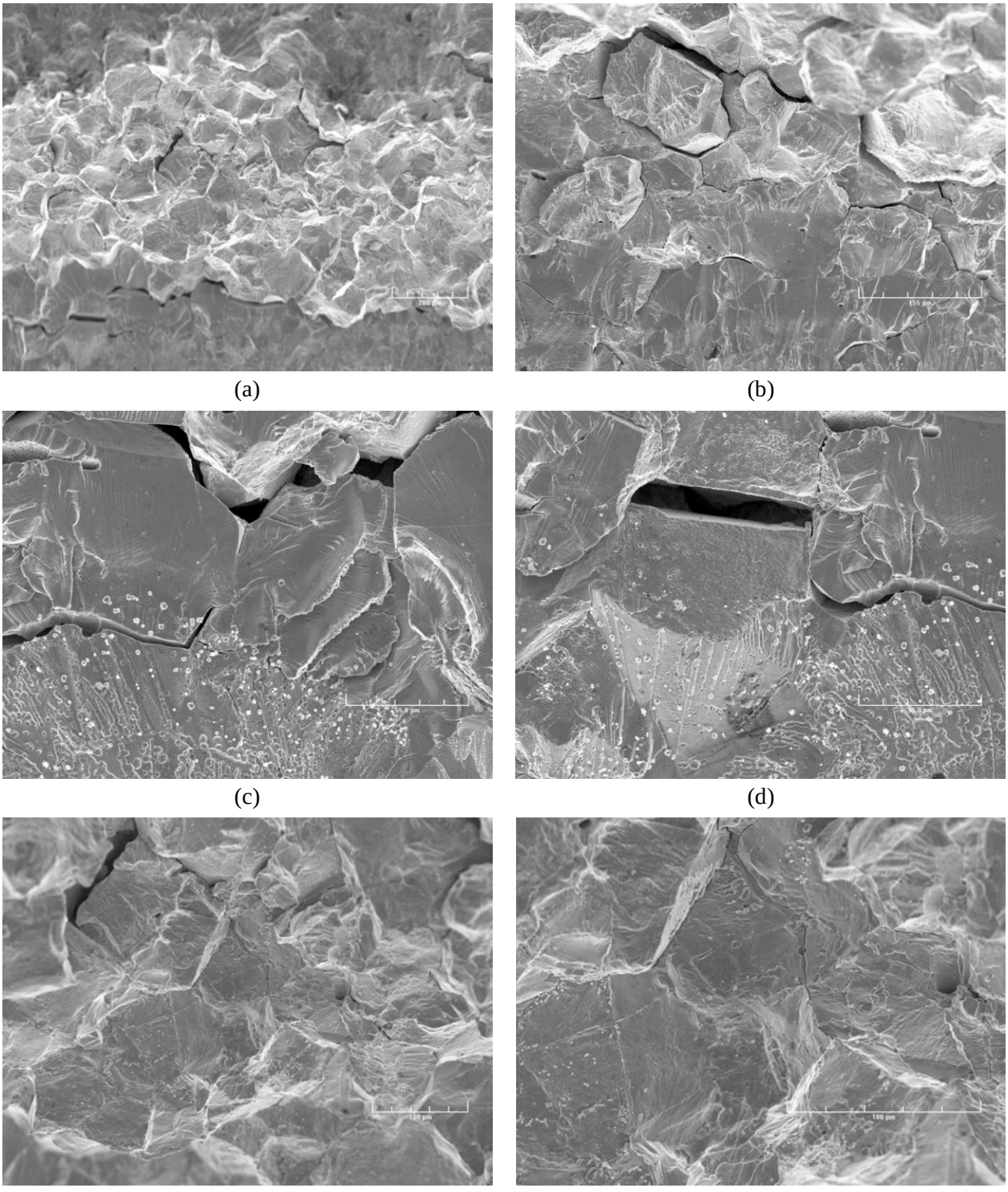

Figure 52. Typical fracture morphologies (a, b) along the change in the fracture plane direction and (c, d) before and (e, f) after the change in direction.

3.2.4.3 Specimen GG3B–A–TT of the HAZ from Grand Gulf Core Shroud H5 SA Weld, Test CGR-14

The environmental and loading conditions, experimental CGRs, allowable values of K_{max} by the K/size criterion, and the deviation of applied K_{max} from the allowable value are given in Table 10. During most test periods, K_{max} was maintained approximately constant by periodic load shedding. The test was started in high–DO water (≈400 ppb DO in effluent) and water flow rate of ≈100 mL/min. The effluent water conductivity and ECPs of a Pt and SS electrode were monitored continuously; the values are listed in the table. The effluent DO level was measured periodically.

Table 10. Crack growth results for Specimen GG3B–A–TT[a] of Type 304L HAZ in high–purity water at 289°C.

Test Period[b]	Test Time, h	Cond.,[c] µS/cm	ECP[c] mV (SHE) Pt	ECP[c] mV (SHE) Steel	R Load Ratio	Rise Time, s	Down Time, s	Hold Time, s	K_{max}, MPa·m$^{1/2}$	ΔK, MPa·m$^{1/2}$	Growth Rate, m/s	Allowed K_{max}, MPa m$^{1/2}$	Deviation in K_{max},[d] %
Pre a	120	0.10	181	20	0.31	0.5	0.5	0	14.32	9.88	7.71E-09	14.4	-1
Pre b	143	0.09	185	25	0.31	5	5	0	14.41	9.95	5.91E-09	14.3	1
Pre c	238	0.08	192	36	0.51	1	1	0	15.02	7.36	1.34E-09	13.9	8
1a*	275	0.07	192	40	0.71	12	2	0	15.95	4.63	8.66E-10	13.9	15
1b*	305	0.07	193	42	0.71	12	2	0	16.31	4.73	2.50E-09	13.7	19
2*	328	0.07	194	44	0.71	30	2	0	16.49	4.78	1.22E-09	13.5	22
3*	403	0.07	195	53	0.70	300	2	0	16.66	5.00	2.80E-10	13.4	24
4*	522	0.07	198	65	0.70	1,000	12	0	16.65	5.00	1.12E-10	13.4	24
5a	580	0.07	203	79	0.70	12	12	3600	16.37	4.91	4.34E-11	13.4	22
5b	765	0.14	202	87	0.70	12	12	3600	16.66	5.00	9.60E-12	13.2	27
6	1,000	0.07	155	42	0.70	500	12	3600	18.52	5.56	9.06E-12	13.1	41
7	1,094	0.07	155	47	0.70	500	12	3600	20.38	6.11	4.47E-12	13.1	55

[a]Nonirradiated Grand Gulf H5 SA weld bottom shell HAZ as–welded plus thermally treated for 24 h at 500°C.
[b]An asterisk indicates environmental enhancement of growth rates under cyclic loading.
[c]Represents values in the effluent. Water flow rate was ≈100 mL/min; the DO level in the effluent was ≈400 ppb.
[d]Based on flow stress.

Precracking was initiated at R ≈0.3, K_{max} ≈14 MPa m$^{1/2}$, and a triangular waveform. After ≈0.4 mm crack advance, R was increased incrementally to 0.7, and the waveform was changed to a slow/fast sawtooth with rise times of 12–1000 s; in all cases time to unload was 2 s. The constant load tests were conducted using a trapezoidal waveform with R = 0.7, 1–h hold period at peak load, and 12–s unload and reload periods. The test was interrupted twice, once at ≈240 h when the hydraulic pump tripped because of an increase in cooling water temperature, and again at 580 h when a power bump caused the hydraulic system to trip. Each time the test was restarted under the loading conditions prior to the interruption. The test conditions, e.g., crack length and growth rates, prior to the interruption were restored after the first restart but not the second restart. The specimen was accidentally overstrained during the second interruption; the crack length increased by ≈0.13 mm after the restart, and the growth rate was a factor of ≈5 lower. To help restore the higher growth rates, a 500–s rise time was added to the loading cycle but with no success. The unusually low CGRs measured during test periods 5b–7 may have been influenced by the accidental overstrain.

After the test, the final crack front was marked by fatigue cycling in air at room temperature. A detailed metallographic evaluation of the specimen was performed to examine the fracture surface and fracture plane morphologies. A 1–mm–thick slice of the entire CT specimen was cut off, and the remainder of the specimen was pulled apart. Composite micrographs of the cross section of the specimen and the fracture surface of the specimen are shown in Figs. 53 and 54, respectively.

In Specimen GG3B–A–TT, fracture seems to have occurred along two planes. These two fracture planes overlap in the specimen cross section shown in Fig. 53. Also, note that the crack extension represented by the noncorroded fine cracks on the right occurred during fatigue cycling at room temperature to mark the final crack front. The final crack extension as measured by SEM was ≈30% greater than the value determined from the DC potential measurements. Crack extensions estimated from the DC potential drop method were scaled proportionately; the corrected values of K_{max} and growth rates are listed in Table 10.

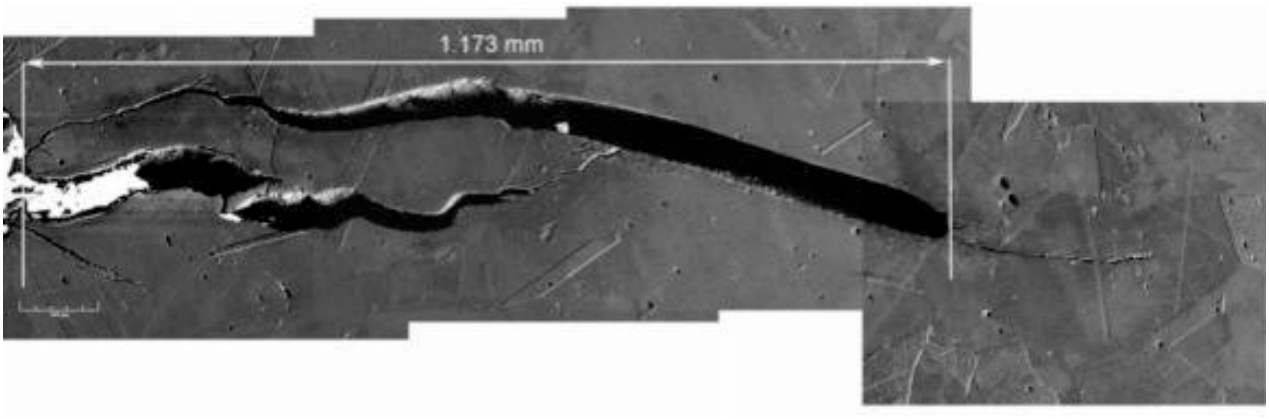

Figure 53. Micrograph of the cross section of Specimen GG3B-A-TT showing the fracture plane profile.

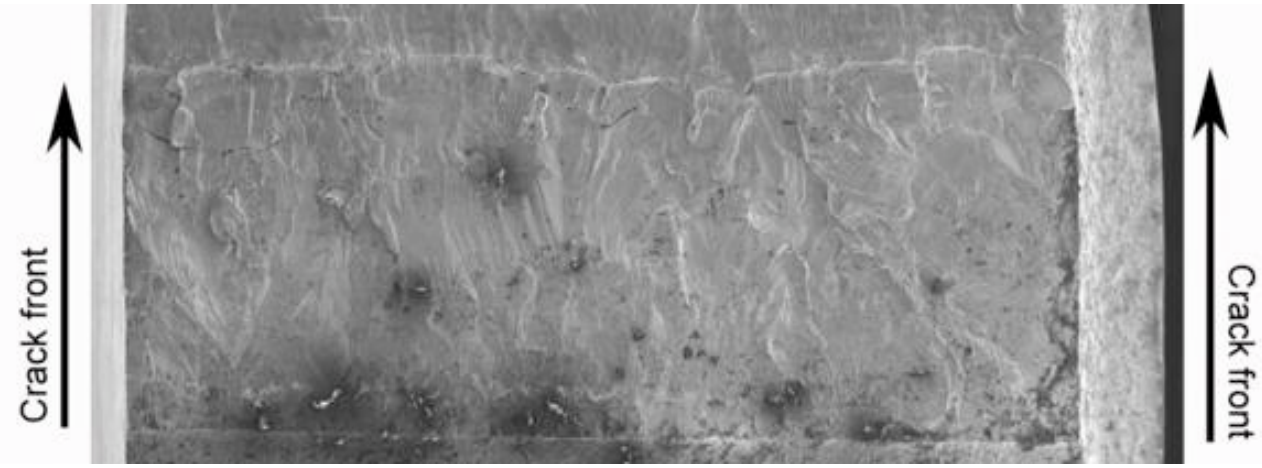

Figure 54. Micrograph of the fracture surface of Specimen GG3B-A-TT tested in high–DO water at 289°C.

The changes in crack length and K_{max} with time during the various test periods are shown in Figs. 55. For this specimen, significant environmental enhancement occurred after ≈270 h when R was increased from 0.5 to 0.7 (Fig. 55b). Also, the results in Table 9 indicate that for this specimen, the K values during precracking and up to test period 5 were 15–27% higher than the K/size criterion of Eq. 9, and 40–55% higher than the allowed value for periods 6 and 7.

Micrographs showing a slice of the entire crack extension and typical fracture morphology at select locations on the surface are given in Fig. 56. This specimen was not cleaned chemically to remove the surface oxide film. Once again, a predominantly TG fracture morphology is evident for the entire crack extension. Most of the TG facets show a well–defined river pattern.

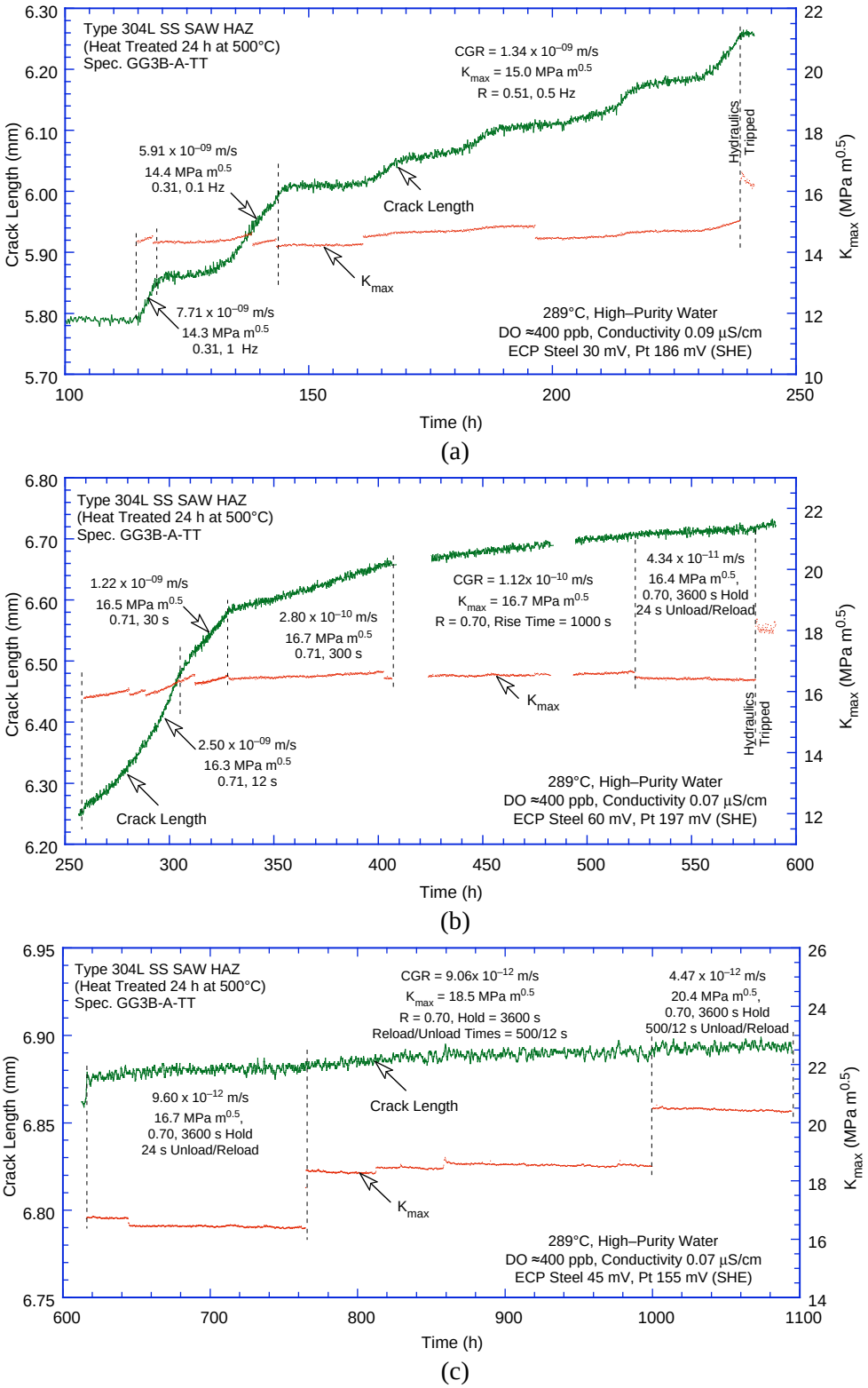

Figure 55. Crack length vs. time plots for nonirradiated thermally treated Type 304L bottom shell HAZ from the Grand Gulf H5 SA weld in high–purity water at 289°C during test periods (a) precracking, (b) 1-5, and (c) 5–7.

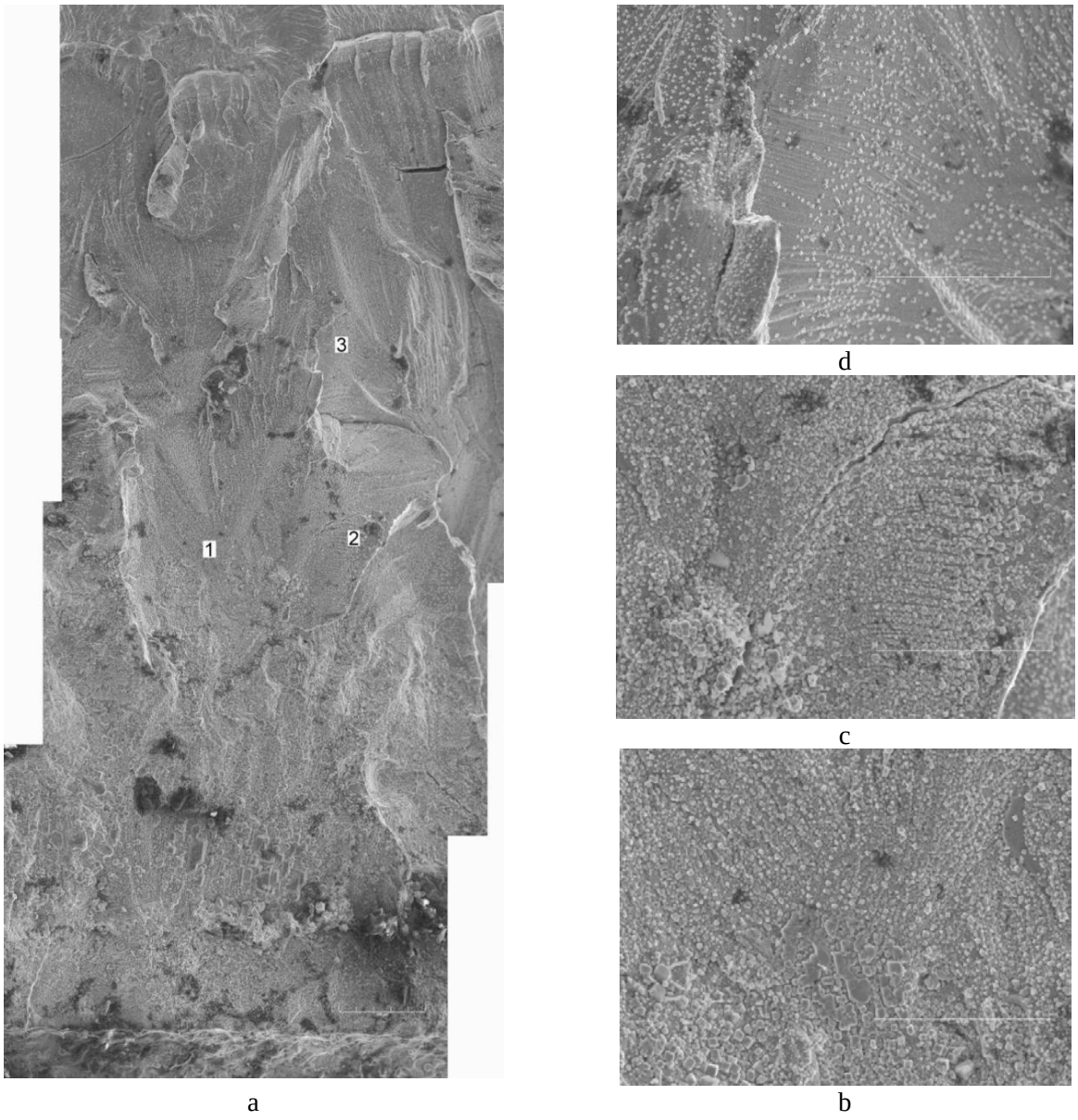

Figure 56. Micrographs showing (a) slice of the entire length of the fracture surface and (b), (c), and (d) high-magnification micrographs of the fracture surface at locations 1, 2, and 3, respectively.

3.2.4.4 Austenitic SS Weld HAZ under Continuous Cycling

For continuous cyclic loading, the experimental CGRs for nonirradiated SS weld HAZ specimens in high–DO environment and those predicted in air for the same loading conditions are plotted in Fig. 57. The uppermost curve represents the Shack/Kassner model for nonirradiated austenitic SSs in high–purity water with 8 ppm DO (Eq. 7). The CGRs in air $\dot{a}_{air}$ (m/s) were determined from the correlations developed by James and Jones,[69] e.g., Eqs. 3–5.

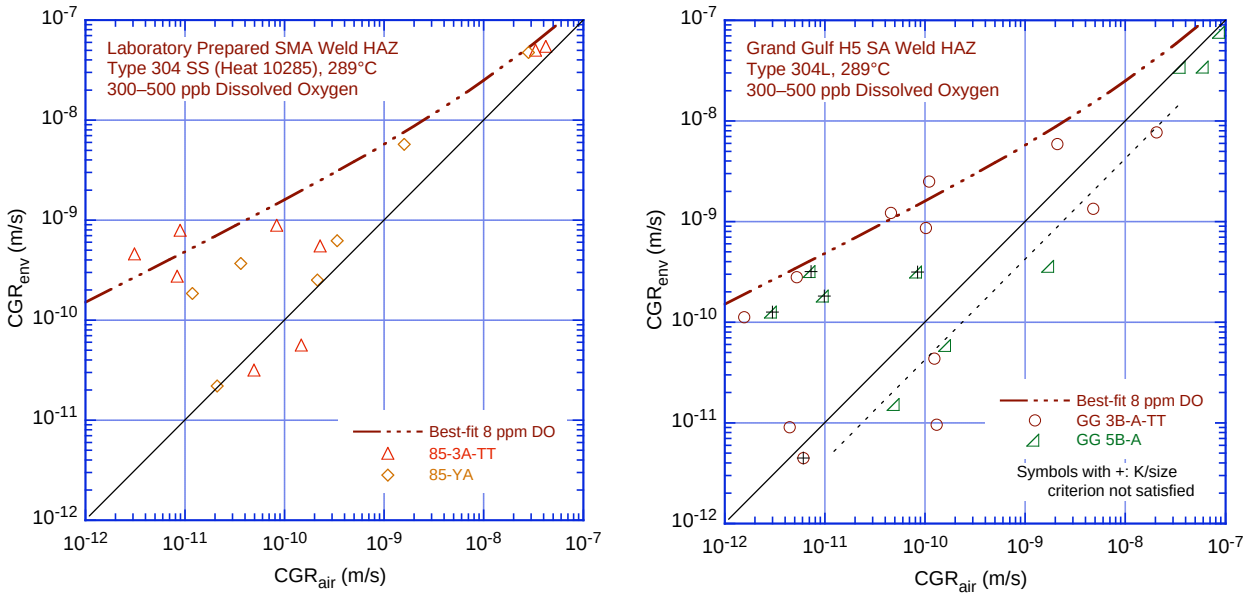

(a) (b)

Figure 57. CGR data for nonirradiated specimens of (a) laboratory–prepared Type 304 SS SMA weld HAZ and (b) Type 304L SA weld HAZ from the Grand Gulf core shroud under continuous cycling at 289°C in high–purity water with 300–500 ppb dissolved oxygen.

In these figures, the data points that lie along the diagonal represent predominantly mechanical fatigue, and those that lie close to the Shack/Kassner model indicate environmentally enhanced crack growth. For both irradiated and nonirradiated specimens, enhancement of CGR did not occur readily when the load ratio and rise time were increased. For example, a large number of data points lie along the diagonal in Fig. 57, particularly for the GG Type 304L weld HAZ. The applied K_{max} had to be increased to observe enhanced growth rates.

The results indicate that under mechanical fatigue loading (i.e., no environmental enhancement), the CGRs for the GG Type 304L SA weld HAZ are lower than those for the Type 304 SMA weld HAZ, e.g., the CGRs for the laboratory–prepared Type 304 weld HAZ (Fig. 57a) show good agreement with the predicted values, while those for the GG weld HAZ are a factor of ≈2 lower (dashed line in Fig. 57b). Also, under this type of loading thermal treatment of the material for 24 h at 500° has little or no effect on growth rates.

In the high–DO NWC BWR environment (the environmentally enhanced condition), the CGRs of the laboratory–prepared Type 304 SS SMA weld HAZ (Fig. 57a) and those of the GG Type 304L SA weld HAZ (Fig. 57b) are comparable. For both GG and laboratory–prepared weld HAZ, the growth rates of the as–welded plus thermally–treated condition (triangles in Fig. 57a and circles in Fig. 57b) are marginally higher than those of the as–welded condition (diamonds in Fig. 57a and right–angle triangles in Fig. 57b). The results for GG weld HAZ are in good agreement with the growth rates obtained by Andresen et al.[72] for GG Type 304L weld HAZ in high–DO water (2000 ppb DO) at 288°C. For example, Andresen obtained a CGR of 3.4×10^{-10} m/s at R = 0.7, K_{max} = 27.4 MPa $m^{1/2}$, and triangular waveform with 500 -s rise time.

Metallographic examination of the fractured specimens indicates that under environmentally enhanced growth conditions (i.e., the data points that lie close to the Shack/Kassner model), an IG fracture morphology is observed for the laboratory–prepared Type 304 SS weld HAZ (Figs. 51 and 52).

Transgranular fracture morphology is observed under conditions that show little or no environmental enhancement (i.e., data points that lie close to the diagonal in Fig. 57a) and are predominantly due to mechanical fatigue. The fracture morphology of GG Type 304L HAZ seems to differ from that for Type 304 SMA weld HAZ. For example, in the GG HAZ, a TG fracture morphology with a well–defined river pattern is observed under all loading conditions, even where growth is environmentally enhanced (Figs. 45 and 56). IG fracture morphologies are usually observed in cold–worked SSs, whether initially annealed or sensitized.[72–74] Because of the residual strain associated with the welding process, the observed TG fracture morphology would not be expected in SS weld HAZ, especially for a case in which the environment enhancement is substantial. The reasons for this unexpected behavior are unclear.

3.2.4.5 Austenitic SS Weld HAZ under Constant Load or Cycling with Long Hold Periods

For CGR tests under constant load or using a trapezoidal waveform with long hold periods (i.e., constant load with periodic partial unloading), the experimental CGRs for nonirradiated SS weld HAZ specimens in the high–DO environment are shown in Fig. 58. The results are consistent with the data obtained under continuous cyclic loading. For nonirradiated Type 304L SA weld HAZ, the CGRs of both as–welded (right angle triangles in Fig. 58) and as–welded plus thermally treated (circles in Fig. 58) material are below the NUREG–0313 curve for sensitized SSs in water with 8 ppm DO. Limited data for the Type 304 SS SMA weld HAZ indicate that the CGRs for nonirradiated HAZ (open triangle in Fig. 58) are higher than those for Type 304L weld HAZ and are above the NUREG–0313 curve. A beneficial effect of reducing the corrosion potential of the environment was observed for the SMA weld HAZ. The fracture morphology is different for the two materials, e.g., TG fracture for the Type 304L SA weld HAZ and IG fracture for the Type 304 SMA weld HAZ.

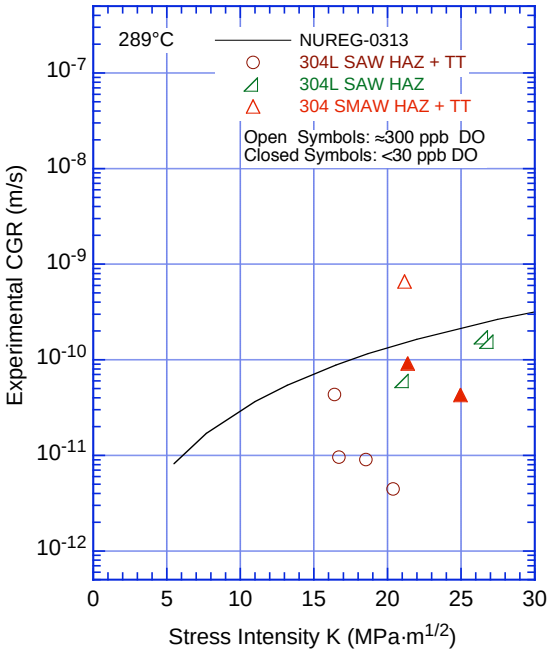

Figure 58.
CGR data under constant load with or without periodic partial unloads for nonirradiated SS weld HAZ specimens in high–purity water at 289°C.